Enhancing in-field current-carrying capability through Ca-doping in BZO-doped YBCO multilayers

Master's thesis
University of Turku
Physics
2025
B.Sc. Caius Condo
Examiners:
Dr. Hannu Huhtinen
Prof. Petriina Paturi

The originality of this thesis has been checked in accordance with the University of Turku quality assurance system using Turnitin Originality Check service.

UNIVERSITY OF TURKU
Department of Physics and Astronomy

Condo, Caius Enhancing in-field current-carrying capability through Ca-doping in BZO-doped YBCO multilayers

Master's thesis, 51 pp.
Physics
April 2025

This study aims to showcase the improvements of barium zirconium oxide (BZO) - doped yttrium barium copper oxide (YBCO) superconductors which can be achieved with 30% calcium-doped YBCO intermediary layers. This study also aims to explain the possible causes for these improvements as they may be useful in designing new and improved coated conductors in high temperature superconductor applications. Two sets of samples were fabricated using pulsed laser deposition. One set of samples were single layered samples with BZO concentrations ranging from 0% to 10% in 2% increments. The second set of samples were the multilayer samples, which had a Ca-doped intermediary layer between the substrate and the first YBCO layer, and another Ca-doped layer between the second YBCO layer. The multilayered sample were also made with varying BZO concentrations in the same way as the single layered samples.

The YBCO thin films were analyzed using x-ray diffraction (XRD) in various measurement modes to achieve thorough information on the structural characteristics and differences the Ca-doping causes. Atomic force microscopy was also used in the structural analysis. The magnetic properties were analyzed using a physical properties measurement system to determine the critical temperature (T_c), critical magnetic field (H_c) and the critical current density (J_c) of the samples. The samples were then patterned using photolithography for further analysis into their current carrying capabilities.

In the XRD measurements we found that the Ca-doping improved the crystalline quality through reduced microstrain in BZO concentrations of 2% and 4%. All multilayer samples experienced narrowing in their $\Delta\phi$ and $\Delta\omega$ values, indicating improved in-, and out-of-plane quality, respectively. Ca-doping also improved oxygen saturation in the samples, as can be seen by a decrease in the ratio between the XRD peak intensities of the (004) and (005) peaks in the 2θ-scan. Improvements in J_c were observed in almost all samples, especially those of higher BZO concentration. Overall the highest absolute J_c values were observed with Ca-doped samples of 0%BZO at low magnetic field strengths and at higher field strengths Ca-doped YBCO with 4%BZO had the highest J_c.

Keywords: High temperature superconductors (HTS), YBCO, multilayers, thin film growth, crystaline quality, flux pinning, critical current density

Contents

Preface

The utilization of superconductors for not only their zero resistance properties, but also their repulsion of magnetic fields, makes them an incredibly interesting material to study and develop. Since the discovery of superconductivity in 1911 [1], the possible applications in energy infrastructure, medicine, transportation, research and other fields have been of great interest. The discovery of high temperature superconductors with critical temperatures above 30 K in 1986 [2], and the subsequent discovery of copper oxide superconductors which can have critical temperatures of up to 92 K has pushed forward the research and application possibilities for superconductors. [3]

Superconductors (SC) have three main parameters that define their behavior, their critical temperature (T_c), critical magnetic field (H_c), and critical current density (J_c). T_c represents the temperature under which a material is superconducting, H_c represents the external magnetic field that the material can withstand before the magnetic flux penetrates the surface and makes the material non-superconducting. The J_c is the maximum amount of current per cross-sectional area that can be transported through the material before it loses its superconductivity. These three values all affect each other. Because of this relation we want our superconductors to have as high critical values as possible, making them far easier to use in a variety of applications.

Rear earth barium copper oxides (ReBCO) are a group of materials that exhibit high temperature superconductivity. One of these materials is the well-known yttrium barium copper oxide or $YBa_2Cu_3O_{7-\delta}$ (YBCO), which has a critical temperature of 92 K [4]. While ReBCO materials have high T_c they are brittle and break easily, this limits how easily they can be used in various applications. This has led to the development of coated conductors (CC), where the superconducting material is grown on a substrate, which helps in the growth and structural resilience of the

conductor.

Type II superconductors can maintain their superconductivity in higher magnetic fields due to them having a mixed state, in which magnetic flux penetrates the material in discrete flux quanta. These flux lines or vortices are moved through the sample due to Lorentz force resulting in resistance in the material. It has been found that defects in the structure of the material can pin these vortices in one place, stopping them from moving and creating resistance. Further study has found that by artificially incorporating defects into the crystal structure of a material we can create pinning centers for the vortices. These artificial pinning centers (APC) increase the H_c of a material significantly, making the application possibilities much more varied. Increasing the concentration of APC has proven to decrease the J_c in zero-field. This is due to the structural deformations/abnormalities they cause. As an example barium zirconium oxide, $BaZrO_3$, (BZO) can be used as an APC in YBCO thin films [5]. The BZO will form nanorods throughout the YBCO, this is referred to as BZO doping. The BZO doping increased the J_c of the YBCO notably in in-field conditions but lowered the J_c in zero-field conditions.

In the specific case of YBCO thin film CC, a Ca-doped YBCO intermediary layer can improve the crystalline growth of the YBCO and BZO nanorods, increasing the zero-field and in-field current carrying capabilities of the thin film [6]. The next step in the research into YBCO thin films is to see how the Ca-doped YBCO intermediary layers affect multilayers of varying BZO concentration. This will be done by controlled fabrication of samples with specific multilayer structure and BZO concentration. The structural properties will be thoroughly analyzed with x-ray diffraction and atomic force microscopy. The magnetic properties will be measured using a physical properties measurement system to determine the T_c, H_c and J_c. The samples will be patterned using photolithography for further analysis into their current carrying properties.

1 Superconductivity

1.1 History

In 1911 when Heike Kamerlingh Onnes was studying the decrease in resistance of metals as they were cooled, he found that when mercury is cooled below 4.2 K its conductivity becomes zero [7]. He named this phenomenon "superconductivity". Superconductivity is a trait that can be found in some materials which in certain conditions allows them to conduct electrical current with no resistance and thus losing no energy to heat. Onnes is credited as the discoverer of superconductivity, he had however, only discovered one of the main properties of superconductors. The second big discovery related to superconductivity came in 1933 by Fritz Walter Meissner, who discovered that superconductors repel magnetic fields when under their critical temperature, thus becoming perfect diamagnets [8]. The qualitative explanation of superconductivity came in 1935 by the brothers F. and H. London. In 1950 Lev Landau and Vitaly Ginzburg proposed a phenomenological model for superconductivity, known as the Ginzburg-Landau theory [9]. Sometime after this, the explanation to the superconductivity of low temperature superconductors (LTS) was developed by Leon Cooper, John Bardeen and John Schrieffer, this is known as the BCS-theory [10]. The discovery of high temperature superconductors (HTS) with critical temperatures above 30 K by George Bednorz and K. Alex Muller in 1986 was the next big step in superconductor development [3]. Quickly after this discovery, new materials were discovered that had critical temperatures above 77 K. The main benefit of these is that the readily available liquid nitrogen boils at 77 K meaning that cooling below the critical temperature is substantially easier than with LTS which require the more expensive liquid helium to get to their critical temperatures [11].

1.2 Theory of superconductivity

The microscopic quantum theory of LTS is described by the Bardeen-Cooper-Schrieffer (BCS) theory. Research into the microscopic quantum theory of HTS is still an on-going field of research. While the Ginzburg-Landau (GL) theory came before the BCS theory, it has proved to be an incredibly useful model for the properties of SC near their T_c. It can also be shown that the GL theory follows the BCS theory in specific temperature and magnetic field ranges.

In a normal conductor, the nuclei of the material can be thought of as points in a lattice and the electrons are moving freely through this lattice. The movement of the electrons is the current. The electrons will collide with the nuclei, resulting in them losing energy. This energy is absorbed by the nuclei and causes heat. This is what the resistance of a conductor is. The BCS theory explains that when we cool a superconducting material below its critical temperature, the electrons stop colliding with the nuclei and form what is called Cooper pairs. These electrons, which normally repel each other due to Coulomb repulsion and electrons having the same negative charge, actually have an attractive interaction when they form Cooper pairs. As the first electron moves through the lattice, it attracts the nearby positively charged nuclei closer together. This creates a higher positive potential area near the first electron, attracting the second electron in that direction. Here, the two electrons form a Cooper pair which acts like bosons, instead of fermions, as electrons normally do. Once the Cooper pairs are formed, they create an energy gap, which is an amount of energy that needs to be acquired by the electrons to break apart the Cooper pair. Cooper pairs are able to traverse the lattice without colliding with the nuclei thus we have current with zero resistance. This is the basis behind the electron-phonon interaction of BCS theory.

The Ginzburg-Landau theory is a phenomenological theory used to describe the electromagnetic properties of SC near their T_c. The main component of the GL

theory is the order parameter ψ, which is the quantum mechanical wave function of the paired electrons. $|\psi|^2$ is proportional to the density of superconducting electrons [12]. Another parameter in the GL theory is the magnetic penetration depth (λ), which describes how far into the SC the magnetic field can penetrate before being fully expelled. The coherence length (ξ) describes the range over which the order parameter can change significantly [13]. The Ginzburg Landau parameter κ defines whether a SC is type I or type II. κ is a ratio between the magnetic penetration depth and coherence length, $\kappa = \frac{\lambda}{\xi}$. Type I SC have a κ value of $< 1/\sqrt{2}$ while type II have a κ value of $> 1/\sqrt{2}$. The GL theory defines the critical fields of a type II SC as

$$H_{c1} = \phi_0/4\pi\mu_0\lambda^2, H_{c2} = \phi_0/4\pi\mu_0\xi^2, \tag{1}$$

where μ_0 is the permeability of free space. The H_c for type I SC is $H_c = \phi_0/4\pi\mu_0\lambda\xi$. From these H_c calculations we can see that the difference in H_{c1} and H_{c2} can be very large leading to varied application possibilities. It is also in this mixed state between H_{c1} and H_{c2} that magnetic flux lines penetrate the SC creating vortices [14].

1.3 Type I and type II superconductors: LTS, HTS

Based on their reactions to magnetic fields, superconductors are divided into two separate categories, type I and type II. Type I SC are usually elemental SC like Pb, Hg and Sn [12]. Type I SC have a relatively low critical temperature T_c at around 10 K or less. They also have a critical field that ranges from 5 to 200 mT [12]. Due to their low T_c and H_c, type I SC are not as easily used in a multitude of applications. Figure 1(a) shows the phase diagram of types I and II SC and (b) shows the magnetization of the SC as a function of applied magnetic field. From these figures, we can see how type I SC only have one H_c, above which they are in their normal state and below which they are in the superconducting state. Type I

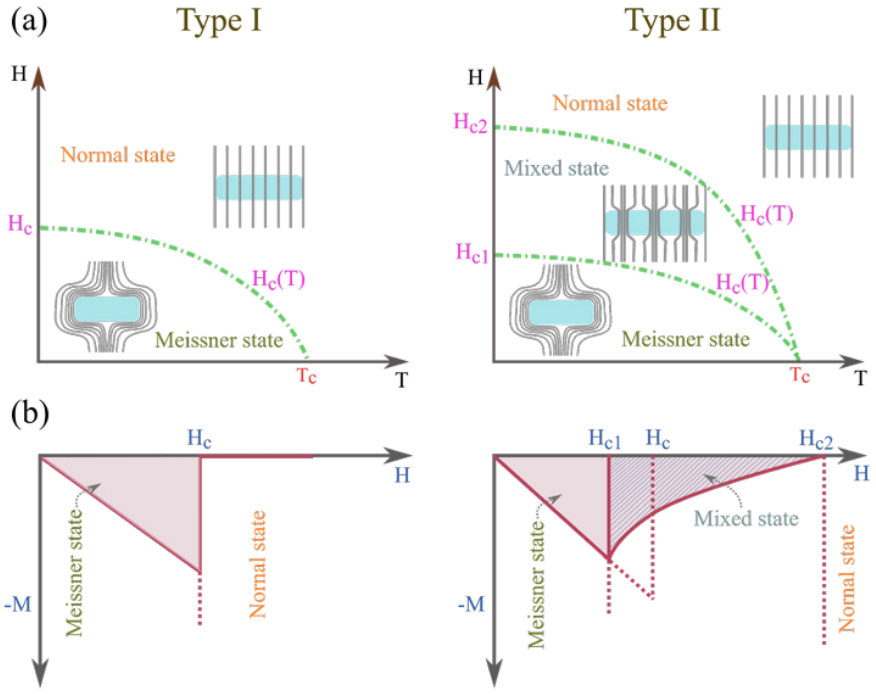

Figure 1. (a) Example of the critical magnetic field dependence on temperature for both type I and type II SC. (b) Magnetization dependence on external field for types I and II. Figure was taken from [14].

SC have a penetration depth of about 50 nm and a coherence length of about 400 nm, this leads their κ value to be much lower than 1.

Type II SC are made of metallic compounds and alloys, as well as oxide ceramics. Type II SC often have a higher T_c than type I SC. They also have two separate H_c values. Below the first H_{c1}, the type II SC behaves in the same way as a type I SC, expelling all magnetic fields and exhibiting perfect diamagnetism. When the H_{c1} is passed, the type II SC does not lose its superconductivity completely, but it allows discrete magnetic flux to penetrate, these are called flux lines or vortices. This is called the mixed state for type II SC, because the SC is still superconducting but is no longer exhibiting the Meissner effect. It is this quality that makes type II SC so useful and varied in their applications. As the magnetic field increases to H_{c2} and above, the SC loses its superconductivity and acts the same way as a type I SC would above its H_c. Because of the much higher H_c and T_c of type II SC, their application possibilities are much larger than those of type I SC. From figure 1(b), we can see how the type II SC H_{c2} value is much higher than the H_{c1} value. This ability of type II SC to withstand large magnetic fields is what makes their application in for example fusion reactors possible.

Another classification method for SC is low temperature superconductors and high temperature superconductors. LTS are SC that have a T_c less than 30 K, while HTS have a T_c greater than 30 K. The discovery of high temperature SC with T_c above 77 K has made research and applications of HTS much easier and cheaper, since the T_c can be reached with liquid nitrogen which boils at 77 K and is much cheaper and easier to produce than liquid helium which is needed for achieving temperatures near absolute zero. A common mistake is to assume that LTS is the same as type 1 SC or that HTS is the same as type II SC. This is incorrect as there are LTS SC that are type II, NbTi for example has a T_c of 9.7 K and can handle magnetic fields up to 10 T, making it a type II SC and a LTS [15].

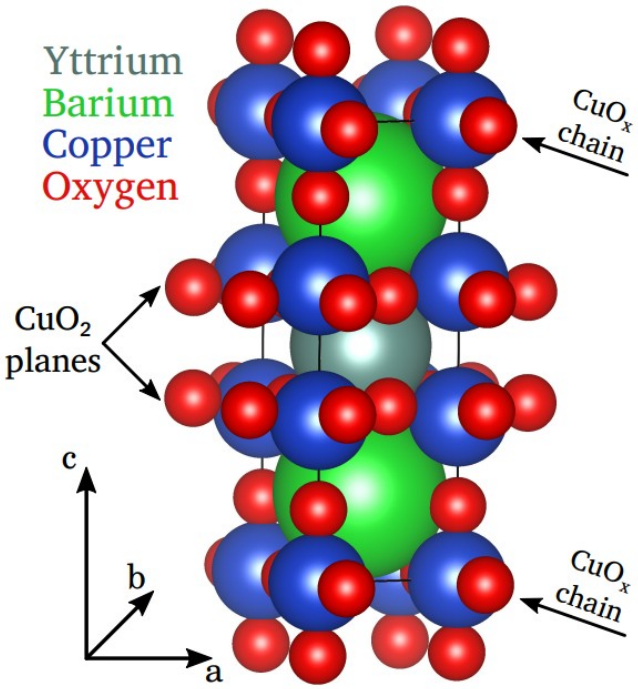

Figure 2. Structural schematic of orthorhombic unit cell of YBCO. The figure is taken from [13].

1.4 YBCO

Yttrium barium copper oxide or $YBa_2Cu_3O_{7-\delta}$ (YBCO) is a rare earth barium copper oxide with critical temperature of 93 K that was discovered in 1987 [4]. The structure of a YBCO unit cell is depicted in figure 2. The molecular structure of YBCO can be divided into three sections, the top, middle and bottom. The top and bottom sections are made up of Ba and CuO_x chain, the middle section is made up of the Y and CuO_2 planes. It is important to note the difference between the CuO_2 planes and CuO_x chains. The supercurrent is carried along the CuO_2 planes and the oxygen site that appear on the CuO_x chains can be either filled or vacant. The notation $YBa_2Cu_3O_{7-\delta}$ is used to describe the amount of oxygen per unit cell, where δ represents the oxygen deficiency. [16]

δ can have a value from 0 to 1, at $\delta = 1$ the molecule is tetragonal and the CuO_x chains are planes, which have vacancies. When δ decreases below 0.65 these

CuO_x planes shift into CuO_x chains, resulting in a molecular structure changes from tetragonal to orthorhombic. This shift makes the molecule superconducting. The orthorhombic YBCO exhibits optimal superconducting properties when $\delta = 0.07$ and the unit cell parameters are $a = 3.8185\,\text{Å}, b = 3.8856\,\text{Å}$, and $c = 11.6804\,\text{Å}$. [17]

YBCO being a type II SC has a mixed state while under its T_c. YBCO is capable of some magnetic flux pinning without artificial pinning centers. In pure YBCO the pinning is usually along structural defects [18]. The incorporation of barium zirconium oxide $BaZrO_3$ in YBCO has shown to improve in-field current carrying capabilities. The BZO grows heteroepitaxially with the YBCO in laser ablated films. These BZO nanorods work as APCs for the vortices that penetrate the sample improving in-field carrying capability. [18]

A drawback of YBCO is its brittle ceramic structure, this is a problem it shares with all HTS materials. This property of YBCO makes it harder to work with when compared to metallic LTS. To combat this problem YBCO has been used in coated conductors, where it is grown as a thin film on a metallic substrate improving its usability in a variety of applications.

1.5 Flux pinning in HTS superconductors

In type II SC when the magnetic field passes H_{c1} magnetic flux lines penetrate the material creating vortices. These vortices experience an attractive interaction towards defects in the crystal lattice. These defects will act as pinning centers, as they will hold the vortex in place with a pinning force (F_p). With current running through the SC the vortices also experience the Lorentz force (F_L), which will cause them to move through the SC when the F_L is larger than the F_p. This is a problem, as the movement of the vortices disturbs the supercurrent, causing resistance resulting in the material no longer being superconductive [12]. Figure 3 shows a schematic of how the magnetic field penetrates the SC material in flux quanta and how the F_L

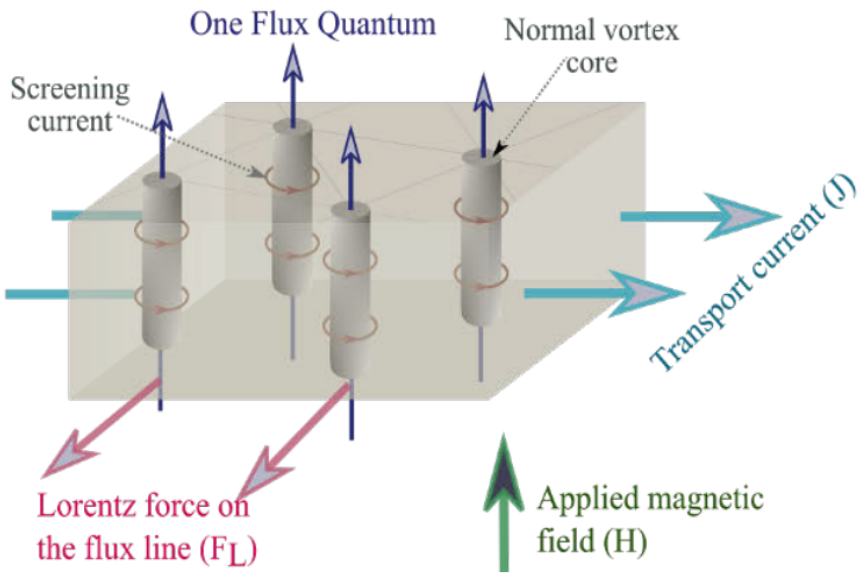

Figure 3. Illustration of flux pinning in type II SC and the relation between transport current, magnetic field and Lorentz force. Image edited from [14].

acts upon the vortices in relation to the transport current and magnetic field.

Naturally occurring defects such as vacancies, dislocations, twin boundaries, stacking faults and grain boundaries act as pinning centers, however their pinning force is weak. The pinning force can be increased substantially by incorporating artificial defects into the SC matrix, these are called artificial pinning centers. Figure 4 shows some of the different types of pinning centers. There are two main categories of APC, uncorrelated and correlated. Uncorrelated APCs are similar to naturally occurring defects in that they form randomly positioned spherical pinning centers that are referred to as nanoparticles. They are much larger than the naturally occurring pinning centers and thus have higher F_p. Correlated APCs are defects that are organized and systematic. These are most often impurities that will stack on top of themselves when grown using deposition methods. Through proper optimization of deposition parameters and selection of materials, correlated APCs can form coherent nanorods that extend through the entire SC film. These nanorods can then effectively pin the vortices in place with high F_p, increasing the H_{c2} and allowing

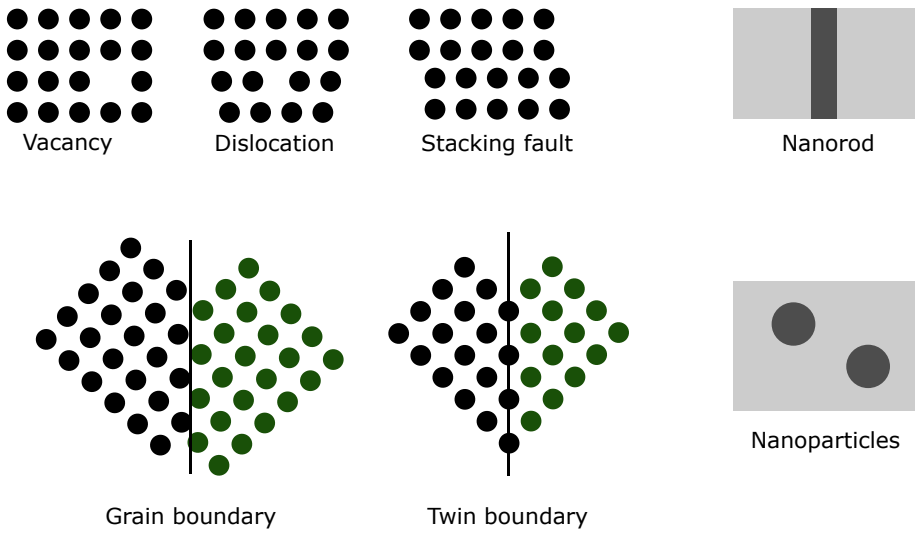

Figure 4. Illustration of lattice defects which can act as pinning centers. On the right, two types of artificial pinning centers, such as nanorods and nanoparticles.

for much more varied applications [13].

As APCs are not superconductive, their incorporation lowers the J_c values at low-fields. This is simply due to the fact that there is less superconductive material, restricting current flow pathways, as well as introducing more strain into the crystal lattice, which further decreases the J_c. Figure 5 shows a schematic of how the J_c value changes as a function of a magnetic field. The black line shows how an APC free SC has higher J_c at low-field, but then drops off quickly as the magnetic field increases. The red line shows a SC with APCs. As seen in the figure, its J_c value at low-field is lower than the APC free SC, but when the magnetic field increases the vortices that penetrate the material are held in place more effectively, resulting in the J_c decrease being much smaller in high-field ranges. In the higher-field ranges where collective pinning occurs, the J_c value follows

$$J_c(B) \propto J_{c,0} \times B^{-\alpha}, \tag{2}$$

where $J_{c,0}$ is the J_c at zero-field and α is a unitless parameter which is associated with vortex pinning [6]. Increasing vortex pinning will decrease α, and decrease the J_c at zero-field.

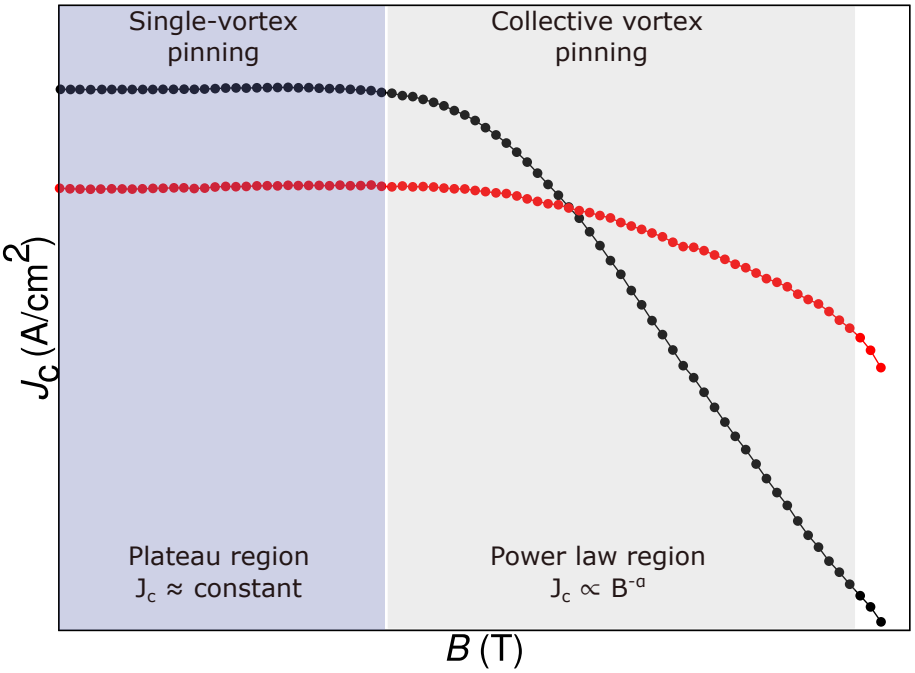

Figure 5. Depiction of critical current density as a function of magnetic field strength of a superconductor without the use of APC (black) and with the use of APC (red).

As mentioned earlier, the J_c at low- and zero-field ranges is mainly determined by the crystal quality of the SC as this is linked to the electron mean free path. APC introduces strain and decreases the crystal quality of the lattice. The use of intermediary layers has been shown to increase the J_c values at low-fields for SC with APCs [6]. The intermediary layer works by relaxing the strain cause by lattice mismatch. As film thickness increases the number of defects also increases. Intermediary layers also work by restarting the growth of the APC containing layers, reducing the number of defects caused by increasing thickness. The use of intermediary layers in SC multilayer thin films is a important design feature when optimizing the J_c of thin film coated conductors.

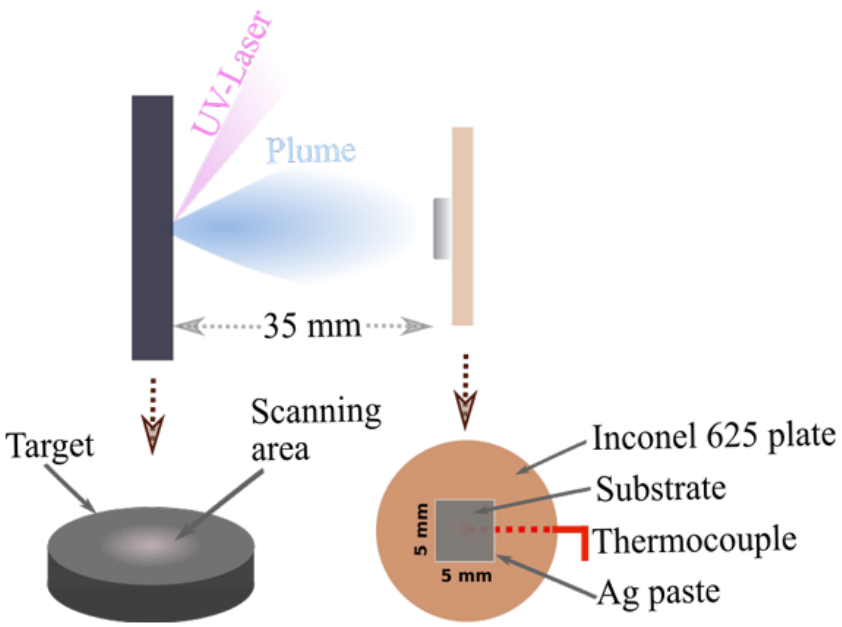

Figure 6. Schematic illustration of the operation principle of PLD. Image was taken from [14].

2 Methods

2.1 Pulsed laser deposition

The superconducting capabilities of YBCO are closely related to its crystal lattice structure. To achieve the best results, the YBCO should be grown epitaxially. This is most easily achieved using pulsed laser deposition (PLD) [19]. PLD is a prominent method of producing epitaxially grown thin films, especially in academic research. The strength of PLD lies in its versatility and simplicity.

The operation principle of PLD is as follows. A high energy laser pulse is directed at a target surface, the energy of this laser causes some of the target material to vaporize resulting in a plasma plume which contains atoms, ions, molecules and particles from the target. This plasma plume travels out from the target surface and when it comes into contact with the substrate, the particles will condense and deposit themselves onto the substrate. The system parameters, such as target to

substrate distance, temperature, laser energy, and pressure affect how the target material is deposited onto the substrate and in turn the crystal quality of the sample [20]. In this work, the PLD parameters were taken from previous research in which the optimized parameters for PLD of YBCO and BZO-doped YBCO were studied [21].

Figure 6 shows a schematic of the PLD process. From the figure one can see the general idea of how the high energy laser causes the vaporized material of the target to form a plasma plume that reaches the substrate surface. One can also see the sample holder to which the substrate is glued onto using Ag-paste and the temperature measuring thermocouple situated in the sample holder.

The target fabrication is not part of this thesis, but put simply the desired components in powder form are weighed and mixed to create a mixture with the desired stoichiometric properties. The mixture is then pressed into a puck and heated to react and sinter it into one solid puck. Targets of pure YBCO, 30%Ca-doped YBCO and BZO-doped YBCO of different BZO concentrations ranging from 0% to 10% every 2% were used.

2.2 X-ray diffraction

X-ray diffraction (XRD) is an immensely useful tool for studying the structural characteristics of a material. Not only is XRD non-destructive, but it also gives us plenty of information about our sample. The way in which XRD works is by first directing x-rays towards the sample at specific angle θ, this is called the Bragg angle. The x-rays will reflect off different lattice planes and the intensity will be measured. Depending on the Bragg angle θ and the spacing between the lattice planes d, the reflected x-rays can interfere with each other, this creates diffraction maxima. Constructive interference happens according to Bragg's law

$$2d\sin(\theta) = n\lambda, \tag{3}$$

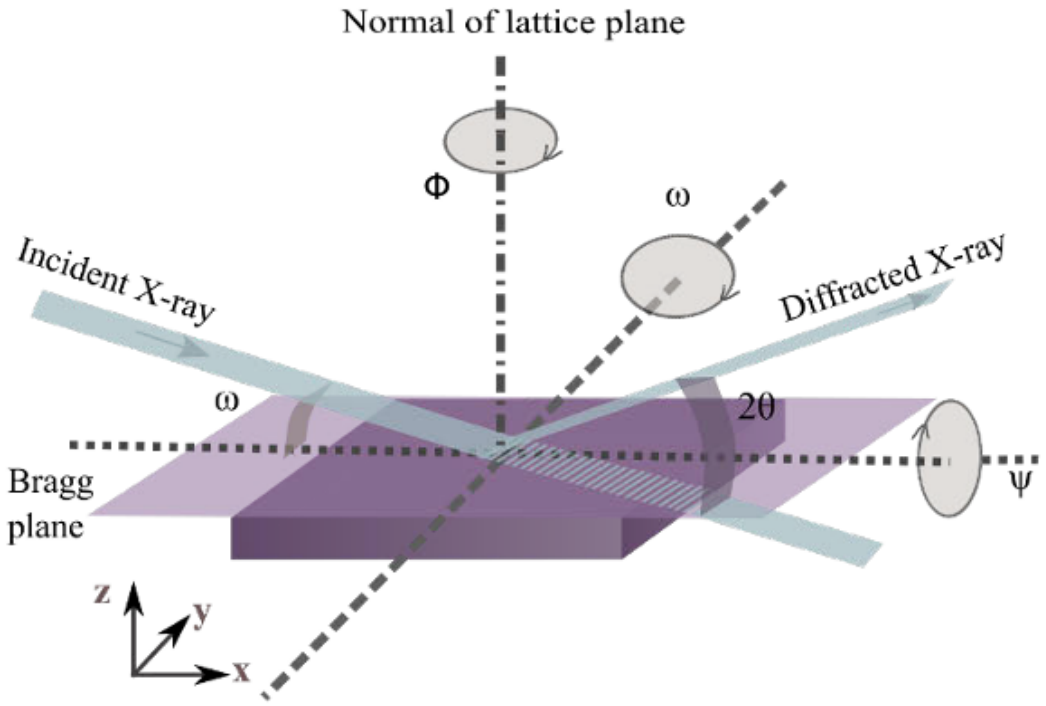

Figure 7. Schematic of used notations for angles and planes in x-ray diffractometer. Image is taken from [14].

where n is the diffraction order and λ is the used wavelength of the x-rays. This equation is the basis for all XRD measurements. [22]

Figure 7 shows the basis for the notations used in this work. Out-of-plane refers to (00l) planes, which are parallel to the sample surface. The in-plane direction is then the (hk0) planes, which are perpendicular to the samples surface. The first measurement which is done is the $2\theta/\omega$-scan. In this scan the sample is fixed in place, and the intensities are measured through varying Bragg's angles. Constructive interference will be seen at specific θ values according to the material being measured. The shape, position, and intensity of these peaks will give us information on the quality of the crystal lattice. Using equation (3), we can calculate the lattice spacing d for our sample. The important results from this scan are which peaks are present, the shape of these peaks and the peak positions. The shift in peak positions of the $2\theta/\omega$-scan is due to residual stresses and substrate induced strain. The

difference in peak shape is due to the size of the grains, compositional gradients, and strain distribution. [22]

The $2\theta/\omega$-scan works as the basis for the next scans, as the $2\theta/\omega$-scan alone does not provide enough information on the structural characteristics of the samples. The rocking curve (RC) or ω-scan is used to judge the quality of the intended epitaxial growth of the sample and its out-of-plane qualities. The ω-scan is performed by positioning the sample at a specific reflection angle from the $2\theta/\omega$ measurement, the sample is then slightly rotated back and forth along the ω axis. The result of this measurement is a single bell curve called the rocking curve. The full width at half maximum (FWHM) is a general indication of the quality of epitaxial growth and by comparing this between different samples we can see how the changes in composition affect the crystal quality.

To further analyze the in-plane characteristics of the sample, a ϕ-scan must be done. The first step in a ϕ-scan measurement is to fix the sample to a specific reflection angle, similar to the rocking curve. The sample is then tilted along the ψ axis and rotated a full 360° along the ϕ axis. A full rotation is done for each angle that the sample is tilted along the ψ axis. The result is an intensity map as a function of tilt and rotation. With this we can determine the characteristics of the sample in all three principal axes.

In this work XRD measurements were performed using the PANalytical Empyrean diffractometer. The x-ray source was the Empyrean tube Cu LFF HR (CuK_α = 1.54060 Å) at 45 kV and 40 mA.

2.3 PPMS: magnetic and resistivity measurements

Magnetic measurements were performed on the samples in order to determine their critical temperature, superconducting transition width (ΔT_c) and to study their behavior at varying temperatures and magnetic field strengths. The measurements

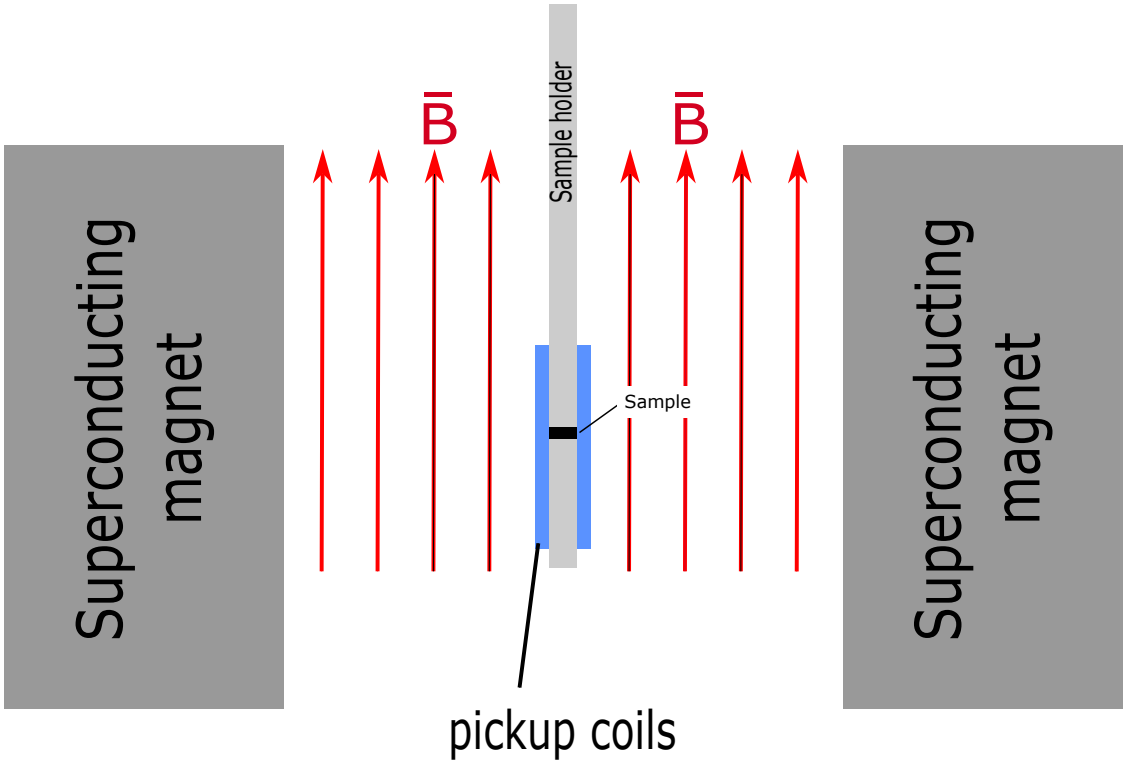

Figure 8. Schematic of main components of PPMS.

were performed with a physical properties measurement system (PPMS) made by Quantum Design using the ACMSII option. A schematic of the PPMS can be seen in figure 8. The main components of the PPMS are the superconducting magnet, which generates a high uniform magnetic field, the temperature controller, and the pickup coils. The pickup coils are situated inside the SC magnet near the sample, this allows precise detection.

The T_c of each sample was measured by means of magnetization as a function of temperature. An AC field was applied to the sample with a frequency of 113 Hz, the sample was also cooled from 95 K down to 10 K. The T_c value was determined by the deviation of the real and imaginary parts of the samples' magnetization. The ΔT_c, was determined as the change in temperature in the $M(T)$ graph between zero magnetization and a loss of 90% of the peak magnetization.

To analyze the in-field behavior of the samples, DC magnetic measurements were

performed. In these measurements, a sample is vibrated inside the pickup coils while a DC magnetic field is applied. The movement of the sample induces a voltage in the pickup coils, which is directly proportional to the magnetization of the sample. With this, we can plot $M(H)$, where M is the magnetization of the sample and H is the applied field. The applied field is slowly changed from 9 to -9 T and back again. This gives us the hysteresis loops of the samples, from which we can calculate the J_c value using the Bean model [23]

$$J_c = 2\Delta m/(a(1 - a/3b)V), \tag{4}$$

where Δm is the opening of the magnetization hysteresis loops, a and b are the width and length of the sample and V is the volume. The thickness of the samples was measured using atomic force microscope after the patterning had been done, with the thickness as well as the length and width the volume was easily calculated.

The resistivity of the samples was also measured as a function of temperature. This was done after the patterning process. The samples were patterned using photolithography, in order to have controlled current flow path ways. Contacts were made using a wire bonder for the resistivity measurements. Resistivity was measured with a standard four-probe method in the PPMS using the resistivity option. From the results, we can see at what temperature the samples gain zero resistivity and thus their T_c.

2.4 Patterning of films: photolithography, AFM

Some measurements require the films to be patterned so that we can have control of current flow and contrast between the deposited material and the substrate surface. We used a photolithography process to pattern our films. The process is illustrated in figure 9. The pattern was designed to maximize YBCO surface area for wire bonding, while having current bridges for controlled current pathways. In the photolithography process, the samples are coated with a photoresist and then they are

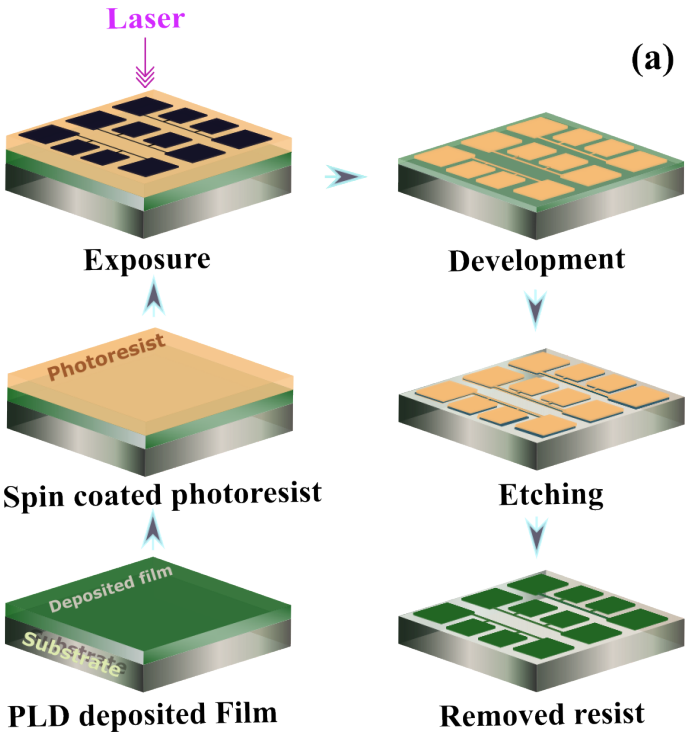

Figure 9. Schematic of the photolithography process, image modified from [14].

exposed to ultraviolet (UV) light. A mask can be applied between the sample and the UV light source so that some areas are not exposed to it, or a laser writer can be used which focuses the UV laser onto only specific parts of the sample achieving the same result. We used a laser writer for the UV exposer. After the exposure, the samples are developed, causing the photoresist to wash away from the UV-exposed areas. Once developed, the sample is etched using an acid to wash away the exposed parts of the sample where there is no photoresist anymore. Lastly the sample is washed in acetone to remove the photoresist from the patterned sample.

The atomic force microscope (AFM) is a device used to analyze the surface microstructure of samples. The main operating principle of a AFM is that a very thin and sharp needle is dragged or tapped along the surface of a sample. The needle is attached to a cantilever which has a laser pointed at its back side which is reflected into a photodiode to measure the changes in the laser position. As the needle moves along the surface of the sample it moves up and down along the contours causing the

reflected lasers position to change. The changes in the reflected laser are analyzed and mapped, giving us a rendering of the surface of our sample.

3 Results and discussion

3.1 Samples

3.1.1 Preparation of samples

Using PLD, we created six multilayer samples and seven single layer samples. All of the samples are grown on a $SrTiO_3$ (STO) substrate. Using PLD the single layer samples were made with 1800 pulses, with a frequency of 5 Hz and laser energy of 64 mJ. The single layer samples were 30% Ca-doped YBCO, 0%-, 2%-, 4%-, 6%-, 8%- and 10% BZO-doped YBCO. The multilayer samples are made with 200 pulses of the Ca-doped YBCO followed by 900 pulses of a specific concentration of BZO-doped YBCO, then another layer of Ca-doped YBCO with 200 pulses and lastly another layer of the same concentration of BZO-doped YBCO with 900 pulses. Illustrations of the samples can be seen in figure 10. When referencing a single layer sample, we will simply use the concentration of BZO to differentiate them, as for multilayered samples we will add a "2x" prefix to indicate the multilayered nature of that sample. For example, the single layered sample with 4% BZO will be referenced as 4BZO and the multi-layer of the same BZO concentration will be 2x4BZO. It is important to note that the increase of BZO concentration increases the number of vortex pinning nanorods and not the diameter of them, as can be seen in figure 10.

The PLD method was executed as follows. Firstly, the STO substrate was glued onto the sample holder using an Ag-paste and then set for one hour. The YBCO and, in multilayer cases also the Ca-YBCO targets were placed into the target holder and into the chamber with the sample. The chamber was sealed and pumped to 10^{-4} Torr. Once the pressure reached that point, oxygen flow was let into the

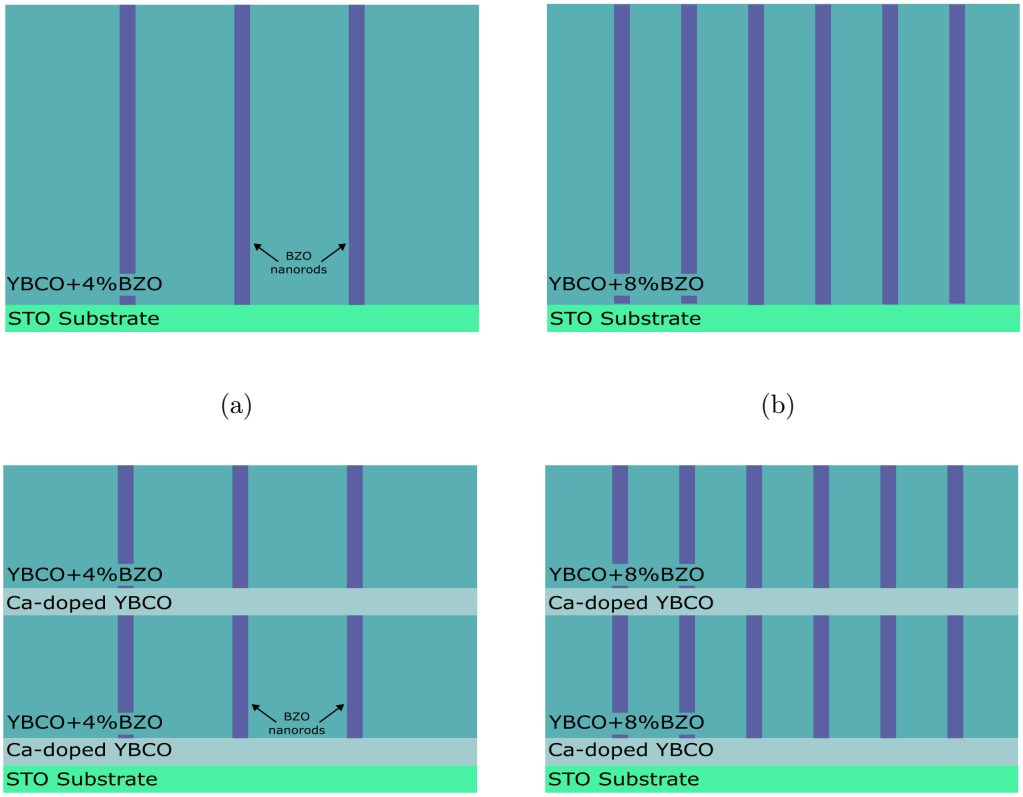

Figure 10. Schematic of the sample layer structure of single layer samples (a) 4BZO, (b) 8BZO, and the multilayer samples (c) 2x4BZO, (d) 2x8BZO.

chamber until the pressure was at 0.175 Torr. Then the infrared laser was turned on to heat up the sample at 25°C per minute, until it reached 750°C. While the sample was warming up, we measured the ultraviolet laser energy to be 64 mJ. Once the sample was at the desired temperature, we turned on the ultraviolet laser and began the pulses. In the case of multilayered samples, after the first set of pulses we would rotate the target holder so that the next target would be in the correct position. The number of pulses was then changed according to which target was in use. The pulses would then be shot at the target. After all the pulses were completed, we would lower the temperature to 725°C and increase the pressure to atmospheric pressure (750 Torr) by letting in more oxygen. The system would then hold the temperature at 725°C for 10 minutes and then lower it to room temperature at 25°C/min. Once the sample had cooled down, we removed it from the chamber and carefully scraped it off of the sample holder with a scalpel, the sample holder was then scraped and sanded clean for the next sample. The targets were removed and sanded down to have a smooth surface and remove the marks created by the ultraviolet laser beam.

3.1.2 Photolithography

To perform more accurate J_c and T_c calculations and angular measurements we must know the thickness of our samples and pattern it to have controlled current flow pathways. Photolithography was used to pattern the films in preparation for resistivity and thickness measurements.

The first step in the photolithography process was making sure the samples would lay flat during the UV exposure. To accomplish this, we checked the back side of each sample for any leftover silver paste, which was used to glue it to the sample holder during PLD. After the back side was sure to be flat, the front side of the sample was washed with isopropyl alcohol. The sample was then spin-coated with a photoresist using a rate of 6000 rpm. After checking that the photoresist had

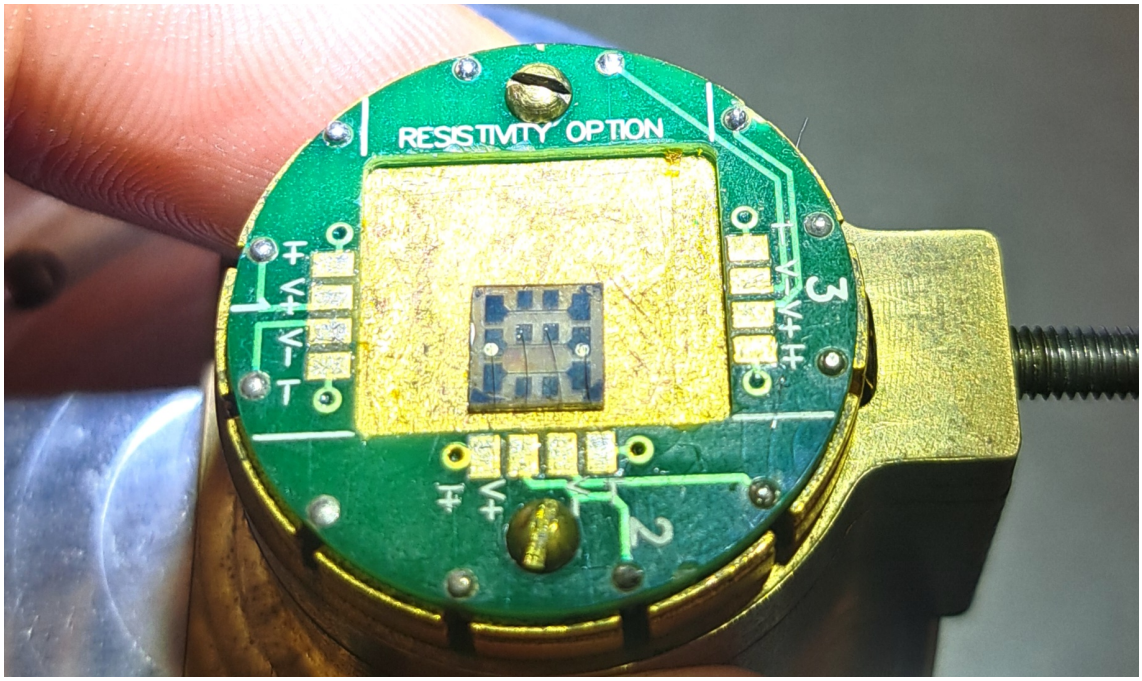

Figure 11. Patterned sample with electrical contacts made on the PPMS resistivity measurement puck in preparation for resistivity measurements. Black pattern on the surface of the 5x5 mm STO substrate is YBCO. Gold contact points were made to assist in wire bonding.

coated the surface of the sample evenly, it was baked on a heating plate at 115°C for 90 seconds. After the baking, it was positioned in a Dilase 250 tabletop laser lithography system, for the UV exposure. After the UV exposer, the samples were then developed in a NaOH solution for about 60 seconds, to remove the exposed photoresist. Once the sample was deemed properly developed and no mistakes were made, it would be etched using a H_3PO_4 solution for about 20 seconds. Lastly the sample would be washed with acetone to remove the leftover photoresist from the surface of the patterned YBCO. The photolithography process was completed in a clean room environment to ensure proper patterning and minimize possibilities of failures.

Before the resistivity measurements could be performed, electrical contacts had to be made. The sample was attached to a puck using double sided tape and then a TPT HB05 wire bonder with 33 μm thick aluminum wire was used to make contacts

from the patterned sample to the puck. Figure 11 shows a picture taken of one of the samples after the wirebonding was completed. Masks were fabricated to direct the gold deposition onto the films. A gold contact point was made because the YBCO tends to break during the wire bonding process. By bonding the wire to a gold surface that is half on the STO substrate and half on the YBCO, we can avoid the risk of breaking the YBCO.

3.1.3 AFM

Once the samples were etched, we could measure their thickness. Using AFM, we could measure the surface of the samples, specifically the difference in height between the substrate surface and the YBCO current bridges. We used a Bruker Innova AFM on contact mode with a scan range of 90 μm, 128 lines back and forth at 0.5 Hz. Results of the AFM measurements can be seen in figures 12 and 13. From these graphs, we can see the bottom level being the substrate surface level and the bump being the YBCO. From the figure, we can see that the substrate surface is at zero nm. Then on the YBCO surface we get values of around 250 nm. This is in line with the thickness we expected to see.

During the AFM measurements, we found that the surfaces were very rough as can be seen in figure 13. The small spikes that appear on the surface may be caused by multiple reasons. One reason could be that the etching process was too short leaving behind small portions of YBCO that were not etched away properly. Another contributing factor could be that the BZO does not react to the acid in the same way as YBCO, thus the BZO can be left behind even after the YBCO has been etched off. The Ca doping could have a similar effect as the BZO. Dust and scratches also contributed to some of the surface abnormalities on the samples. For more accurate measurements, we could have measured multiple different parts of the sample and compared the results. Most of the samples did not have many clean

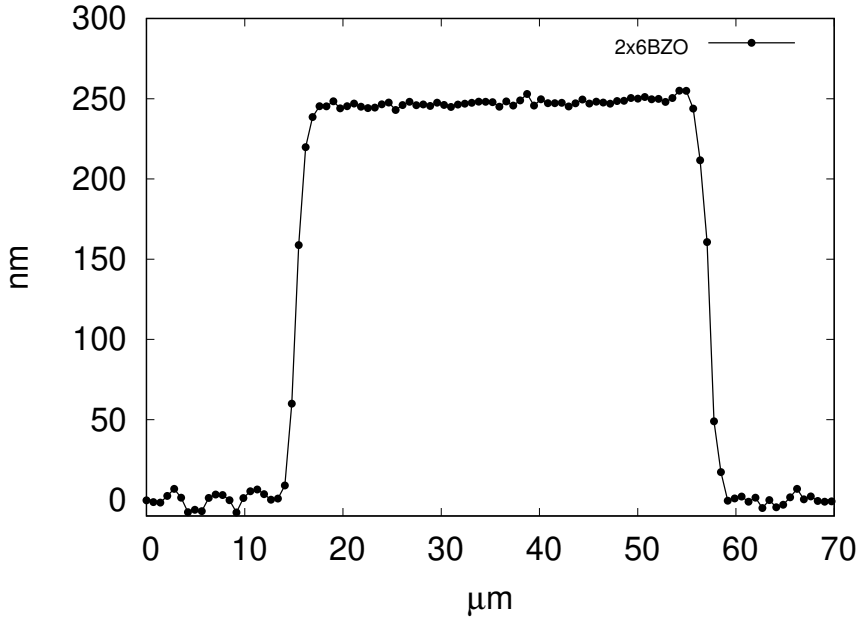

Figure 12. Height profile AFM result measured over the patterned YBCO stripe for sample 2x6BZO. The result shows that the stripe is $\approx 250\,\mathrm{nm}$ thick and $\approx 50\,\mu\mathrm{m}$ wide. The data has been filtered to remove spikes caused by dust or other particles on the surface.

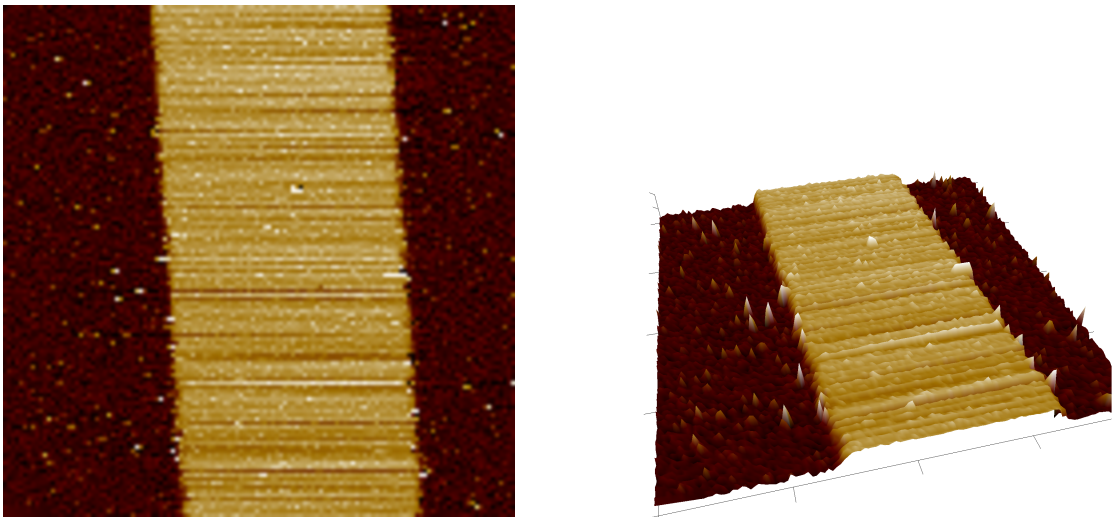

(a) (b)

Figure 13. (a) 2D image from AFM measurements of 2x6BZO. (b) 3D image of the same sample.

areas for AFM measurements and so we have only measured one spot per sample.

3.2 Structural properties of films

3.2.1 X-ray diffraction analysis

Strain within the crystal will cause problems with the crystal growth, the more strain there is the more likely we are to see lattice defects and have improper growth. The main source of strain in our samples is caused by the lattice parameter mismatch between different layers within the structure of the sample. Another source of strain is the increasing concentration of BZO in the YBCO lattice. As mentioned earlier, Ca-doping can improve crystal quality and alleviate some strain, these XRD measurements are done in order to see how this improvement may work with different concentrations of BZO. We will also be comparing the XRD results with the magnetic measurements to see if the improvements in crystal quality are in line with the improvements to the samples superconducting capabilities.

The first XRD measurement which is done is the 2θ-scan. This will give us the baseline for our XRD analysis. From the 2θ-scan we can see peak positions, peak intensities and the peak shapes. We are especially interested in the (004) and (005) peaks as the intensity ratio between these two peaks is called the I_{ratio} and its increase is associated with oxygen deficiency. Figure 14 shows the full 2θ-scan of a few samples for comparison. The small peak seen in the figure at 33° is caused by the reflections of the YBCO (110) plane. This is only seen in higher concentrations of BZO as BZO causes improper growth, resulting in (110) grains not growing epitaxially. BZO growth can be seen by the other small peak on the smaller angle side of the STO(200) peak, at around 43.5°. The blue lines which represent samples with 0BZO do not have this peak. Using the 2θ-scan, we analyzed the FWHM of the (005) peaks ($\Delta\theta_{005}$) to gain a general value for the quality of growth in the sample.

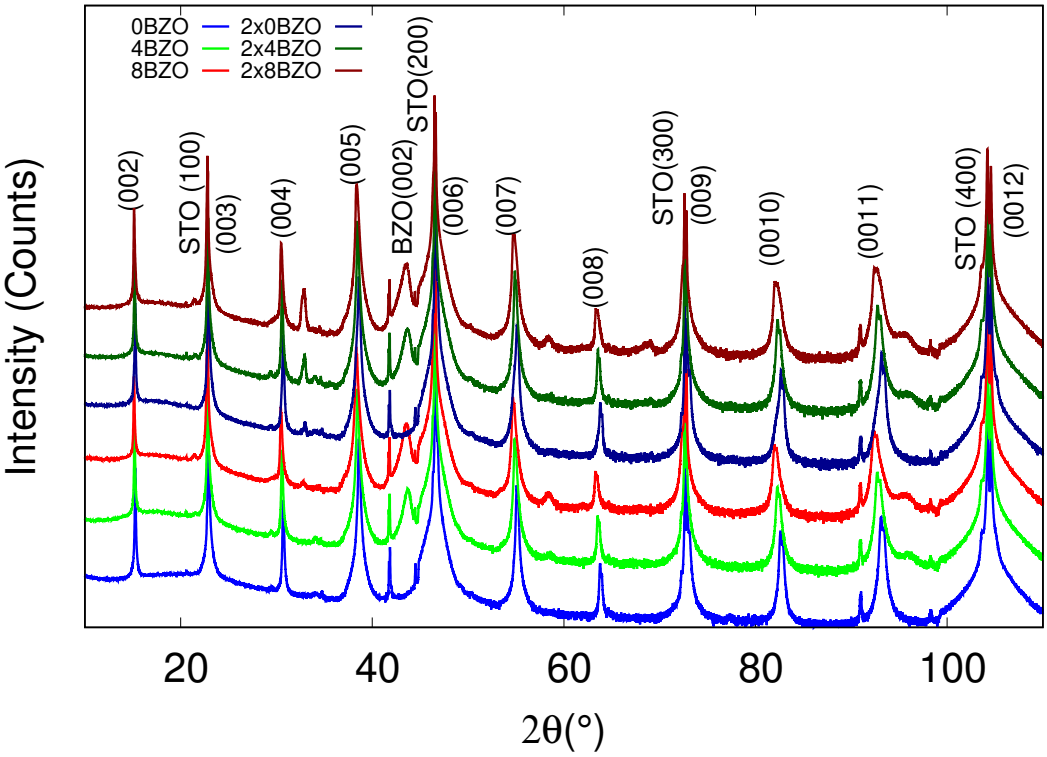

Figure 14. The full 2θ-scan of 0BZO, 2BZO, 4BZO, 2x0BZO, 2x2BZO and 2x4BZO. Peaks have been labeled according to their source. The small peak at 33° is a minor peak caused by reflection of the YBCO (110) plane [24]. Intensity value has been offset to show all results in one figure for comparison.

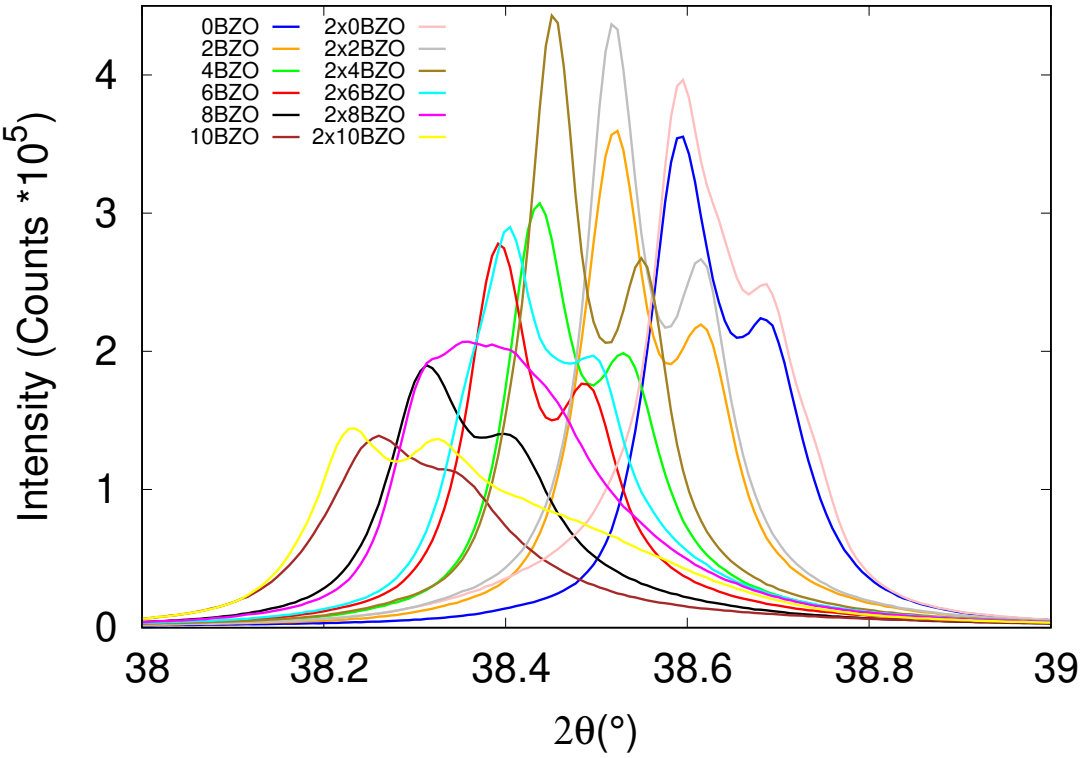

Figure 15. 2θ-scan results focused on the (005) peaks. Clear peak widening and shifting is seen with incease of BZO concentration. Improved peak intensity and width can be seen by comparing single and multilayer results of the same BZO concentration. The x-ray source produces characteristic x-rays of different wavelengths, the primary wavelength is the Cu $K_{\alpha 1}$ which causes the higher peaks, while the lower peak is caused by $K_{\alpha 2}$ which has a slightly shorter wavelength [22]. The difference in peak shapes seen in the 2x8BZO sample is due to the multilayered nature of the sample. The two layers are reflecting the x-rays in a way where the resulting peaks are on top of each other resulting in a rounded peak.

The XRD measurement results are better at medium θ angles, this is one of the reasons we focus on the (005) peaks. The main reason we focus on the (005) peaks is because they have the highest intensity and do not overlap with the STO peaks. When assessing the strain values using the Williamson-Hall (WH) method, we must analyze peaks from the whole 2θ-scan range. The additional layer and Ca-doped YBCO layers distort the peak shapes in the multilayered samples, making peak selection for the WH-analysis more difficult, which increases the error.

Figure 15 shows the 2θ-scan results for the (005) peaks. From the figure, we

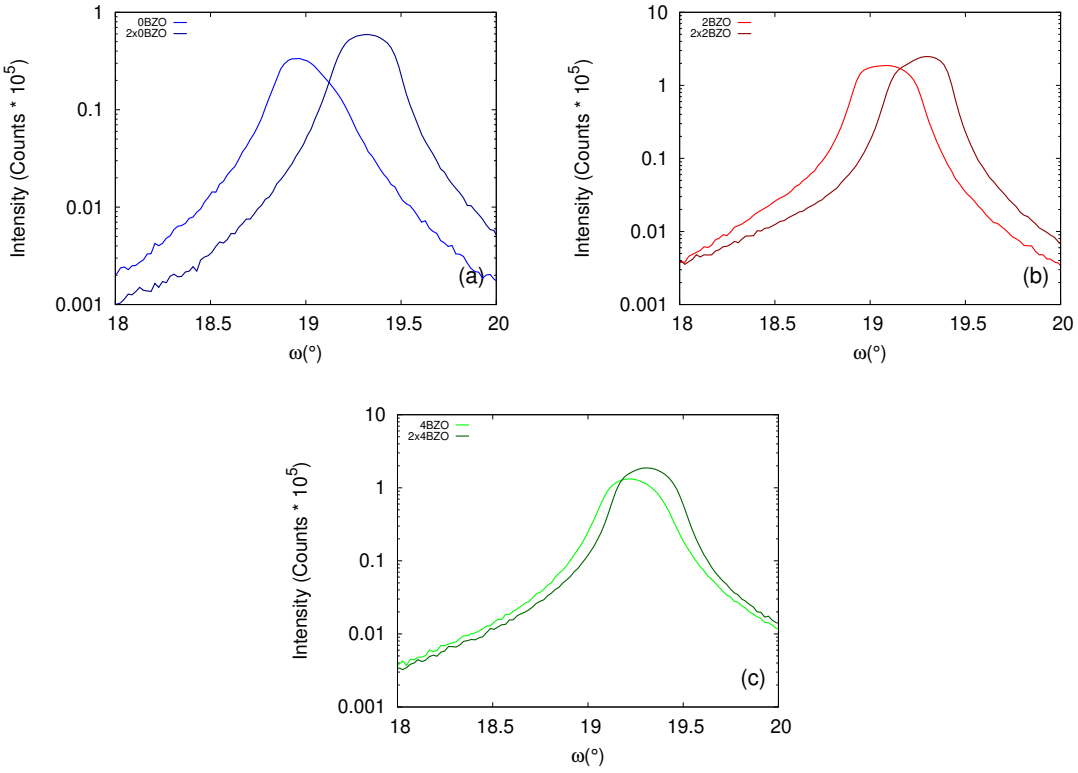

Figure 16. Rocking curve results for (005) peaks of a) 0BZO and 2x0BZO b) 2BZO and 2x2BZO c) 4BZO and 2x4BZO. Multilayer samples show improved peak intensity

can see a clear shortening and widening of the peaks as the concentration of BZO increases. There is also a clear shift in peak positions. The shifting of the peaks is caused by uniform strain. The shortening and widening of the peaks is caused by microstrain. We can see from figure 15 how the multilayer sample peaks are taller than the single layer sample peaks. This indicates better crystal growth in the multilayered samples.

Figure 16 shows the rocking curves of six different samples. As seen in the figure, the multilayer samples have a higher peak and slightly narrower shape, this indicates improved crystal growth in the samples with the Ca-doped intermediary layer. The change in RC peak position also is improved in the multilayer samples, indicating a relaxation of the uniform strain. RC were performed on the (005) peaks and the (002) BZO peaks, resulting $\Delta\omega$ values are compiled in table I.

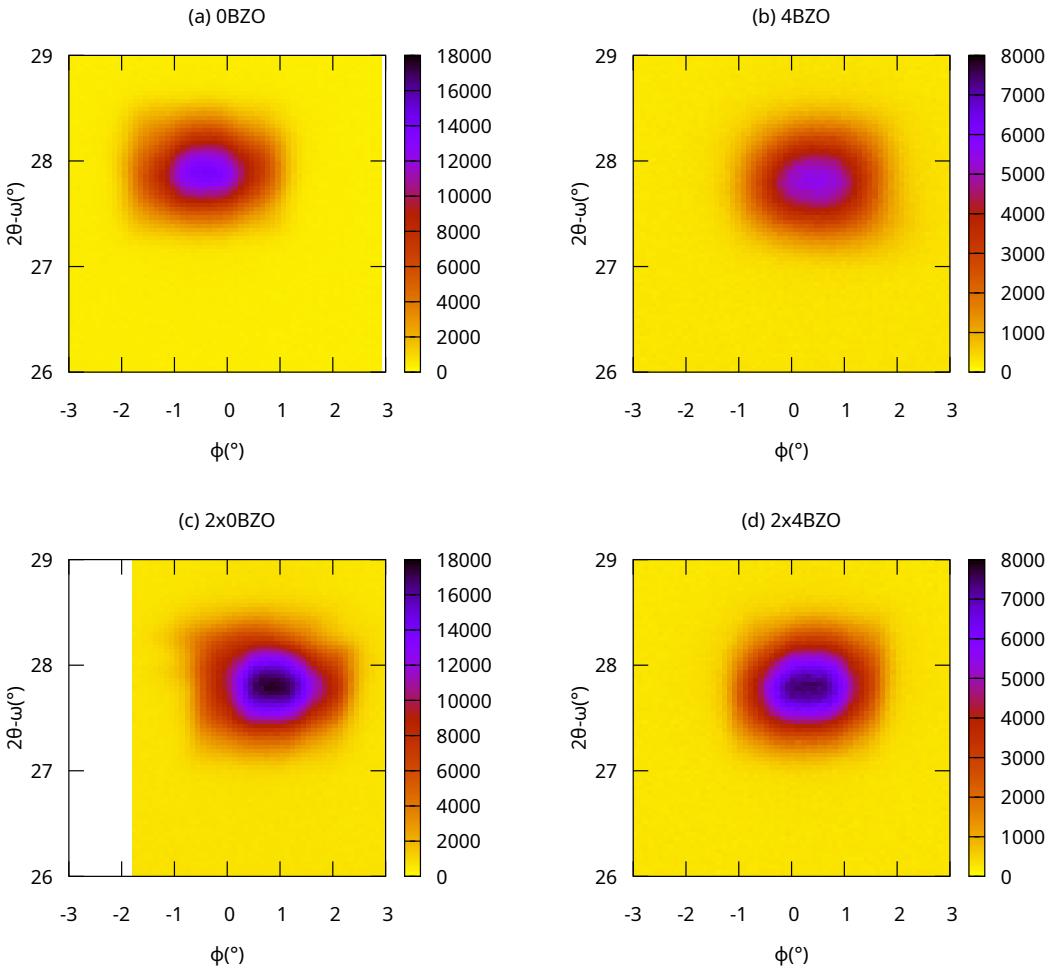

Figure 17. $\phi_{(102)}$-scans of 0BZO, 4BZO, 2x0BZO and 2x4BZO samples. y-axis shows the 2θ value, x-axis is the ϕ value and z-axis is the intensity (counts). Larger intensity maximums can be seen in the multilayer samples indicating higher peaks and thus improved in-plane characteristics.

Table I. FWHM of YBCO 2θ (005) peak, FWHM of YBCO ϕ(102) peak, FWHM of YBCO (005) rocking curve, I(005)/I(004), FWHM of BZO (002) rocking curve, FWHM of BZO ϕ (110) peak and microstrain (ϵ).

Sample	$\Delta\theta_{005}[^\circ]$	$\Delta\phi_{102}[^\circ]$	$\Delta\omega_{005}[^\circ]$	I_{ratio}	$\Delta\omega_{002}[^\circ]$	$\Delta\phi_{110}[^\circ]$	ϵ [%]
0BZO	0.0985	1.9236	0.3248	14.5173	-	-	0.0922
2BZO	0.0944	1.8890	0.3018	14.8554	2.1306	4.6513	0.0933
4BZO	0.0990	1.9171	0.3084	14.4011	2.3465	4.9130	0.1039
6BZO	0.0967	1.9363	0.3008	14.0518	2.4772	5.0272	0.0985
8BZO	0.1331	1.9314	0.4946	14.2379	2.5172	5.0804	0.1543
10BZO	0.1768	2.0773	0.6973	14.2796	2.5383	5.0650	0.2242
2x0BZO	0.1127	1.9380	0.3036	12.3951	-	-	0.0983
2x2BZO	0.0888	1.8609	0.2728	13.9591	2.0377	4.4840	0.0879
2x4BZO	0.0849	1.8633	0.2895	13.7420	2.2558	4.8433	0.0937
2x6BZO	0.1237	1.8894	0.2664	13.2967	2.4658	4.9823	0.1513
2x8BZO	0.1957	1.8684	0.2895	12.6861	2.4444	5.0308	0.2686
2x10BZO	0.3252	1.9242	0.3124	12.8041	2.5165	5.0885	0.4428

To assess the in-plane characteristics of the samples, we performed ϕ-scans for (102) and (212) planes of YBCO and (110) BZO planes. We will use the FWHM of the ϕ_{102}-scan to show the in-plane quality of the samples. The ϕ_{110}-scan will inform us on the BZO growth quality, and the ϕ_{212}-scan will be used in determining the lattice parameters. Figure 17 shows results from the ϕ_{102}-scans of four sample. From this figure, we can see that the intensity maximum is higher in the multilayer samples, as seen by the darker parts in the heat map. This is equivalent to the peaks being higher in the 2θ-scan. The FWHM of the (102) and (110) peaks were calculated and are compiled in table I.

The main results from all XRD measurements can be seen in table I. The first column after sample names is the FWHM for the YBCO (005) peaks. In these

values, we can see that the multilayer samples have smaller $\Delta\theta$ values at BZO concentration of 2% and 4%. A smaller $\Delta\theta$ value indicates a sharper/thinner peak and thus better crystal quality and less microstrain. The last column in table I shows the calculated microstrain values for each sample. When comparing these values to the $\Delta\theta$ values we can see that the microstrain decreases in the multilayer samples of 2BZO and 4BZO, this reinforces the results of improved crystal quality for those BZO concentrations.

$\Delta\phi_{102}$ and $\Delta\omega_{005}$ both show improvements with multilayering. $\Delta\omega_{005}$ improvement indicates better out-of-plane quality, while the improvements of $\Delta\phi_{102}$ indicate improvements of in-plane quality. The I_{ratio} in all multilayer samples is smaller than in the single layer counter parts, this shows an increase in the degree of oxidation in the YBCO lattice. The oxygen atoms in the Ca-doped layer are capable of filling the oxygen vacancies in the weakened YBCO structure near the BZO nanorods. This is the reason for the decrease in the I_{ratio} seen in multilayer samples.

From table I, we can also see the results of the XRD measurements done to analyze the growth of the BZO nanorods within the YBCO. Columns $\Delta\omega_{002}$ and $\Delta\phi_{110}$ show us the FWHM for the peaks of the BZO planes (002) and (110), respectively. The multilayers experience improvements for these values with the exception of the 2x10BZO sample. This shows that multilayering helps in the formation of the BZO nanorods.

To determine the lattice parameters, we analyzed three different lattice planes. As an example, for the 0BZO sample the (005) plane in the 2θ-scan is at an angle of 38.594°. From the ϕ-scans we found that the 2θ value for plane (122) is 55.496° and for plane (212) it is 55.135°. With these three different peaks we were able to calculate the lattice parameters $a = 3.87\,\text{Å}$, $b = 3.86\,\text{Å}$ and $c = 11.65\,\text{Å}$. In the ϕ-scans the peaks resulting from the (122) and (212) planes are quite close together. At low concentrations of BZO the peaks are clearly defined from each

Table II. Lattice parameters of the samples.

Sample	a [Å]	b [Å]	c [Å]
Ca-YBCO	3.88	3.83	11.69
0BZO	3.87	3.86	11.65
2BZO	3.87	3.86	11.68
4BZO	3.89	3.84	11.70
6BZO	3.88	3.85	11.71
8BZO	3.86	3.86	11.73
10BZO	3.86	3.86	11.75
2x0BZO	3.89	3.83	11.65
2x2BZO	3.88	3.82	11.68
2x4BZO	3.89	3.84	11.70
2x6BZO	3.89	3.85	11.71
2x8BZO	3.86	3.86	11.72
2x10BZO	3.86	3.86	11.74

other. As the concentration increases the peaks get closer together until they can not be differentiated from each other. This is a result of the a and b lattice parameters approaching the same value as the crystal structure becomes less orthorhombic.

Comparing the lattice parameters from table II, we see that in the multilayer samples the lattice parameter a is bigger at low concentrations of BZO when compared to the single layer samples. The lattice parameter b is smaller, at low concentrations of BZO, in the multilayer samples than in the single layer samples. Both lattice parameters approach the same value. Comparing the c values we see very little difference between single and multilayer samples. Multilayer samples have smaller c values at the higher concentrations of BZO. From these we can see a small increase in the in-plane quality of the crystal.

The STO substrate has a cubic structure and a lattice parameter of a=3.905 Å. YBCO has lattice parameters of $a = 3.82$ Å, $b = 3.89$ Å, and $c = 11.68$ Å [17, 25]. The mismatch of the lattice parameters between YBCO and STO causes strain in the system. From table II, we can see that the Ca-doped YBCO has lattice parameters that are closer to those of STO. Because of this, the mismatch in lattice parameters is made smaller, decreasing strain and improving crystal growth.

To summarize this section, the incorporation of Ca-doped intermediary layers improves the out-of-plane characteristics of all the samples as seen in the $\Delta\omega_{005}$ results. Multilayering also improved oxygen saturation in all samples. For in-plane results the $\Delta\theta_{005}$ and microstrain values were only improved by multilayering in 2% and 4% BZO concentrations. Improvements were also seen in the ϕ_{102} values for all multilayers except for the 0BZO case. BZO growth quality was improved in multilayers as seen by the decrease in $\Delta\omega_{002}$ and $\Delta\phi_{110}$ values, with the exception of the 10BZO samples.

3.2.2 Effect of Ca-doped YBCO spacer on improved film growth

Improvements in the crystalline quality of YBCO thin films are directly related to the improvements of their J_c in zero-field. Multilayering has been shown to increase J_c in previous studies [26–28]. The Ca-doped YBCO intermediary layer improves crystalline quality in two ways. The first way is that it relaxes the strain caused by lattice mismatch, giving the BZO-doped YBCO a smooth epitaxial interface to grow on [6]. Defects caused by BZO growth in the YBCO matrix increase as the film thickness increases. The addition of an intermediary layer relaxes this strain and gives the next layer of BZO-doped YBCO a smooth surface to start the growth again. The vortex pinning BZO nanorods may not be perfectly on top of each other throughout the multilayers, which would reduce the effective pinning force of the sample. However the improvements in crystal quality may make up for this by significant improvements in the $J_{c,0}$.

The second mechanism in which Ca-doped YBCO layers help the crystal quality is improving the YBCO quality near the BZO nanorods. YBCO quality suffers near the BZO nanorods due to the lattice mismatch. Strain and misfit dislocations at the BZO and YBCO boundaries lead to an increase in oxygen vacancies. The mobile oxygen atoms from the Ca-doped YBCO layer can migrate to these vacancies fixing some of the defects, resulting in improved crystal quality and thus improved J_c. This is in line with the decrease in I_{ratio} that we observed in the XRD section, as the decrease in I_{ratio} indicates higher oxygen saturation in the YBCO lattice. The level of oxygen saturation of the YBCO lattice has a direct effect on the superconducting properties. The Ca-doped layer has brought these levels closer to optimal [17]. Figure 18 showcases the proposed improvement mechanisms caused by the Ca-doped YBCO intermediary layer [6].

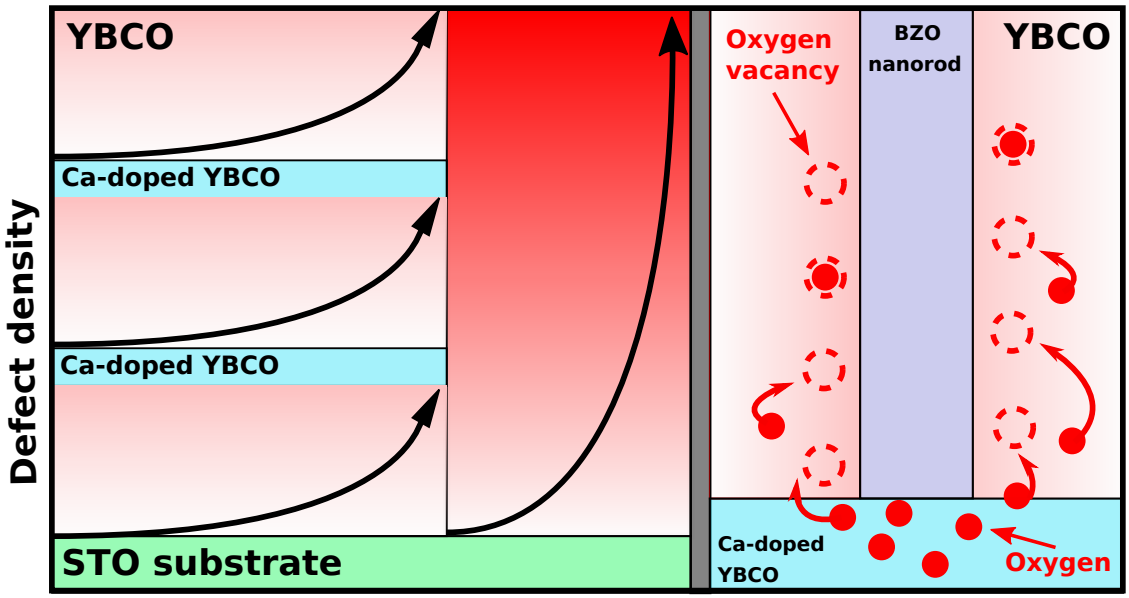

Figure 18. Illustration of proposed mechanisms behind the improvements as a result of Ca-doped YBCO intermediary layers. The left image shows how the intermediary layer helps with strain relaxation and reduces the total number of defects that occur when compared to a single layer. Image is taken from [6], so the layer structure is different from the samples in this work but the mechanisms are the same. The image on the right depicts the mobile oxygen atoms from the Ca-doped layer migrating to the vacancies near the BZO nanorods.

3.3 Superconducting properties

3.3.1 Temperature dependence of magnetization

Figure 19 shows us the onset of the superconducting phase of our samples at very low magnetic field. Figure 19(a) displays single and multilayered samples with BZO concentrations from 0% to 4% and (b) shows from 6% to 10%. The magnetization of the sample going from 0 to -1 indicates its transition into the superconducting state, as it begins to expel magnetic fields and transforming into a perfect diamagnet. This method was used to define the onset critical temperature of each sample at zero-field. At low concentrations of BZO, the single layer samples have higher and thus better T_c compared to the multilayered samples. At concentrations of 4BZO and above the multilayer samples have higher T_c than the single layer sample of the same BZO concentration. ΔT_c depicts the minimum temperature change when going from normal state to superconducting state.

Note that during the execution of the magnetic measurements there were some issues with the temperature measuring parts of the PPMS in the ACMSII option. Due to this, the specific temperature values reported in figure 19 may not be as precise as we would normally want. However, since the error would be the same for all samples the difference in temperature should be accurate.

3.3.2 Resistivity measurements

Figure 20 shows the measured resistivities of the samples as a function of temperature. The T_c decreases as BZO concentration increases. This is expected as the incorporation of BZO into the lattice causes strain and decreases crystal quality. From the figure, we can see at what temperature each sample's resistivity becomes zero thus determining their T_c. When the concentration of BZO is low, 0–4%, the single layered samples have higher T_c. When the BZO concentration goes above 6%, the multilayers have a higher T_c. This is likely caused by the fact that at low BZO

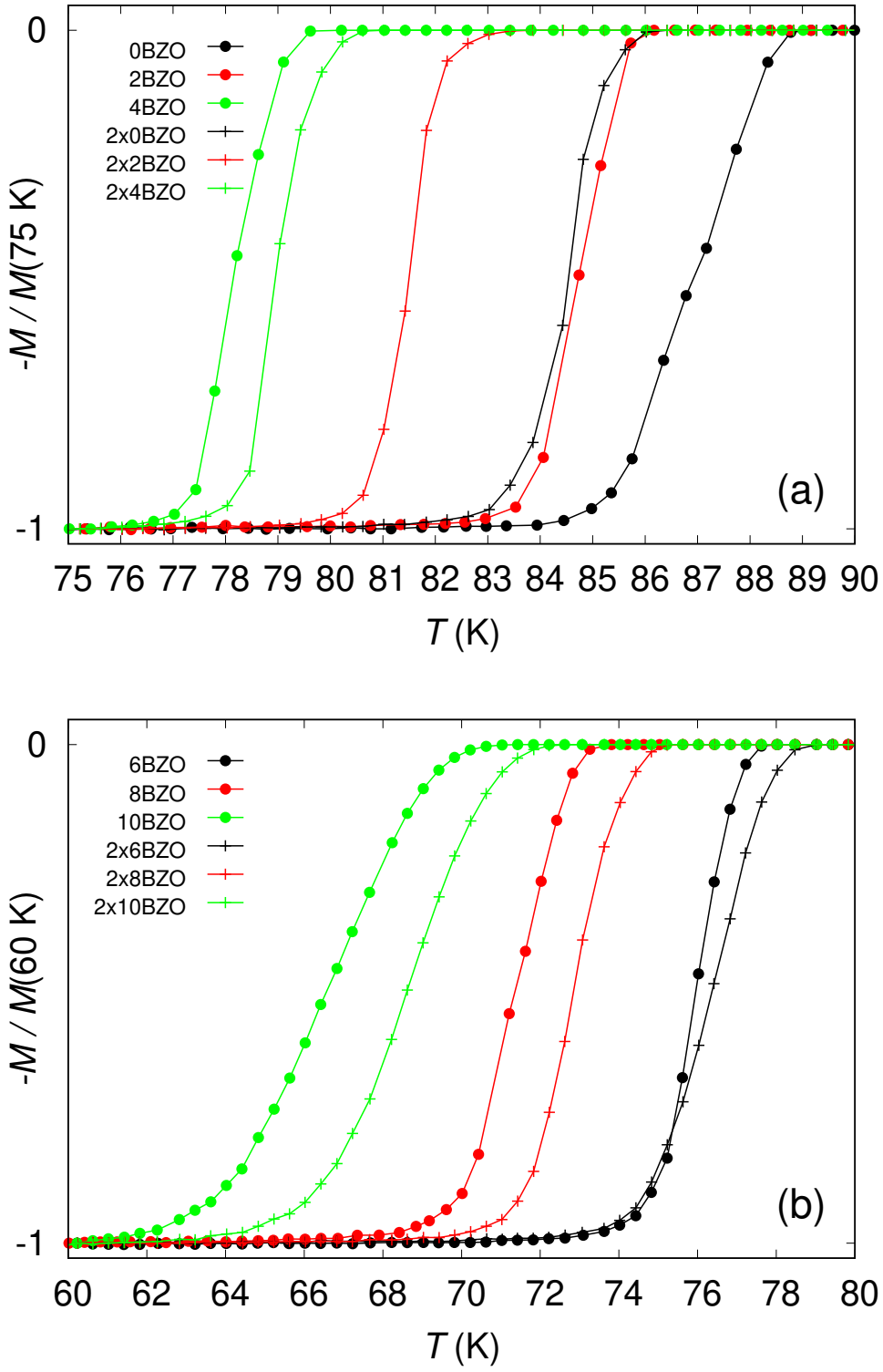

Figure 19. Temperature dependence of magnetization in (a) samples with BZO concentrations of 0%, 2% and 4%, (b) samples with BZO concentrations of 6%, 8% and 10%. Magnetization has been normalized for a clearer image.

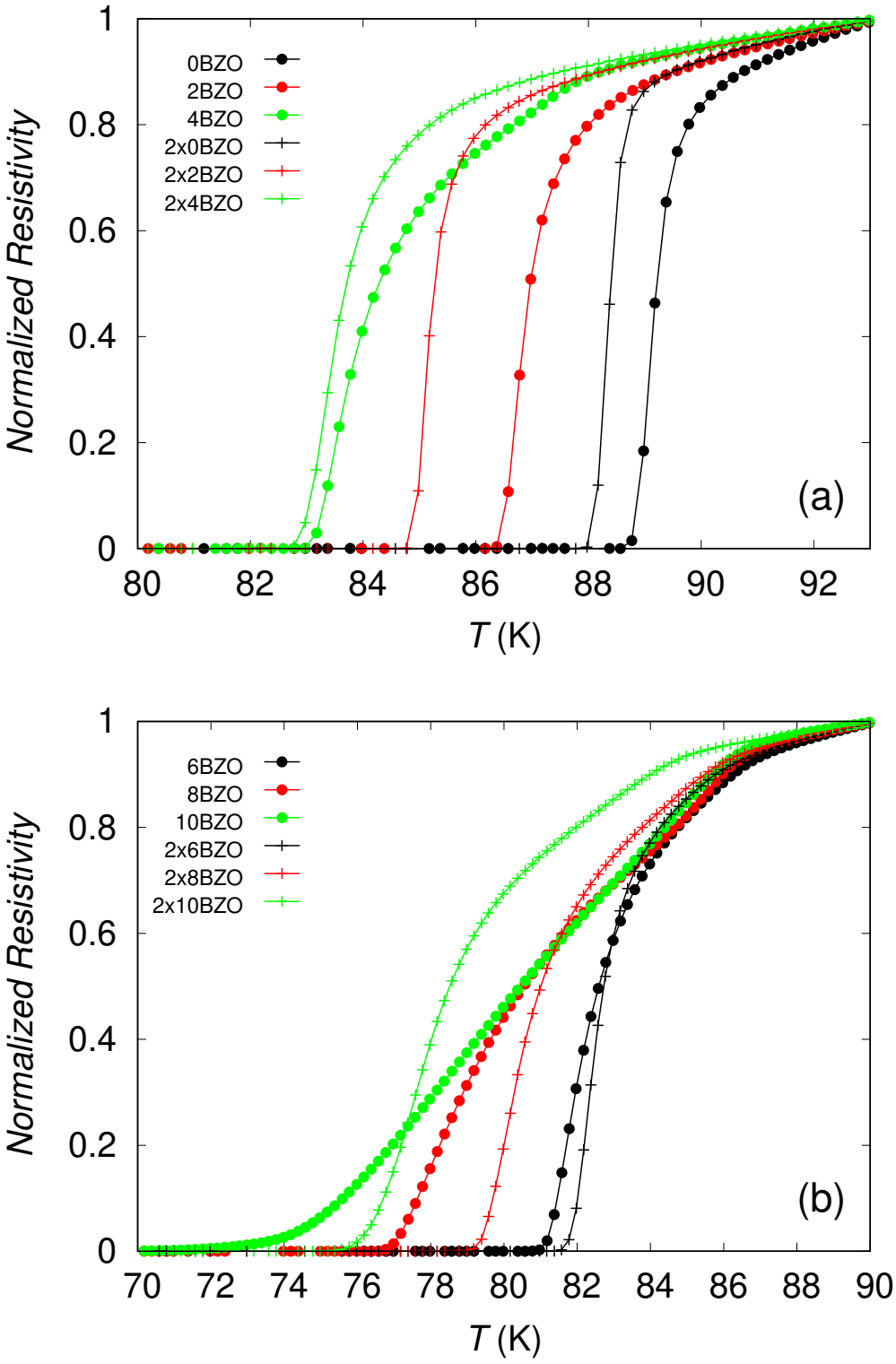

Figure 20. Resistivity measurements as a function of temperature to determine the T_c of the samples. (a) Results from samples with BZO concentration of 0%, 2% and 4%, (b) Results of samples with BZO concentration of 6%, 8% and 10%.

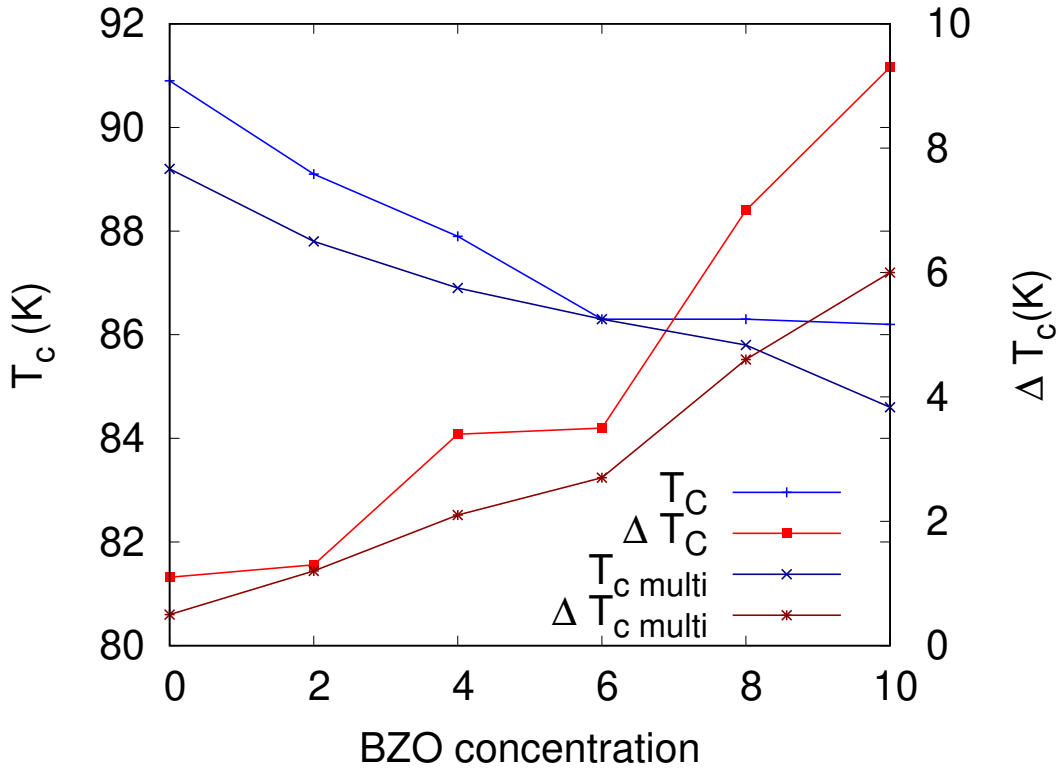

Figure 21. Onset T_c and transition width (ΔT_c) values as a function of BZO concentration.

concentrations the quality of the crystal lattice is still good and so the Ca-doped layer is not fixing many defects. As the BZO concentration increases, there are an increasing number of lattice defects and thus improper growth. It is here, where the Ca-doped layer can prevent these defects thus improving the crystal quality. Multilayering seems to improve the ΔT_c in all samples, but more clearly at higher BZO concentrations.

When comparing these T_c results to the ones achieved in the magnetic measurements section, the main difference is that the resistivity measurements resulted in higher T_c values. This is because of an issue with the temperature measuring parts of the ACMSII, the details of which we will not go into other than to say the absolute T_c values are more accurate in the resistivity measurements than they are in the magnetic measurements.

From figure 21, we can see how the increasing BZO concentration affects the

onset T_c and ΔT_c values. Single layer samples had higher onset T_c at all BZO concentrations, but they also had higher ΔT_c values. The ΔT_c value was calculated by observing the temperature change from when the resistivity changes from 90% of what it was at onset T_c to 10% of what it was at onset T_c.

3.3.3 Critical current densities

With the data from the PPMS measurements and using the Bean model [29], we were able to plot out the critical current density as a function of the applied magnetic field. Figure 22 shows the $J_c(B)$ relations of all samples at varying magnetic fields and temperatures. The same ranges and scale have been used in all the pictures of figure 22 for ease of comparison. We can see the expected linear plateau region at the beginning, where J_c is constant followed by the power law region where the J_c begins to decrease. It is clear that at lower temperatures the J_c is higher throughout the magnetic field range than it is at higher temperatures. We can also see that the zero-field J_c decreases as the concentration of BZO increases. The shapes of the J_c curves are important, as we can see the decreasing rate in the power law region is much smaller for samples with higher BZO, this goes to show the improved flux pinning capability and in-field endurance of these samples. Multilayering increased the zero-field J_c of all the samples. 2x0BZO had higher J_c than 0BZO throughout the magnetic field range at all temperatures. At concentrations of 2%, 4% and 6% BZO the difference in J_c of single and multilayers gets smaller as the magnetic field increases. These samples have the smallest improvements in J_c, but have the highest absolute J_c. The greatest improvements in J_c due to multilayering, was experienced by the samples with 8% and 10% BZO. In these samples, the J_c of the multilayer remains higher than the single layer throughout the magnetic field and temperature ranges. The improvements of J_c are in line with the improvements in the I_{ratio} as well as the structural improvements that were seen in the XRD section.

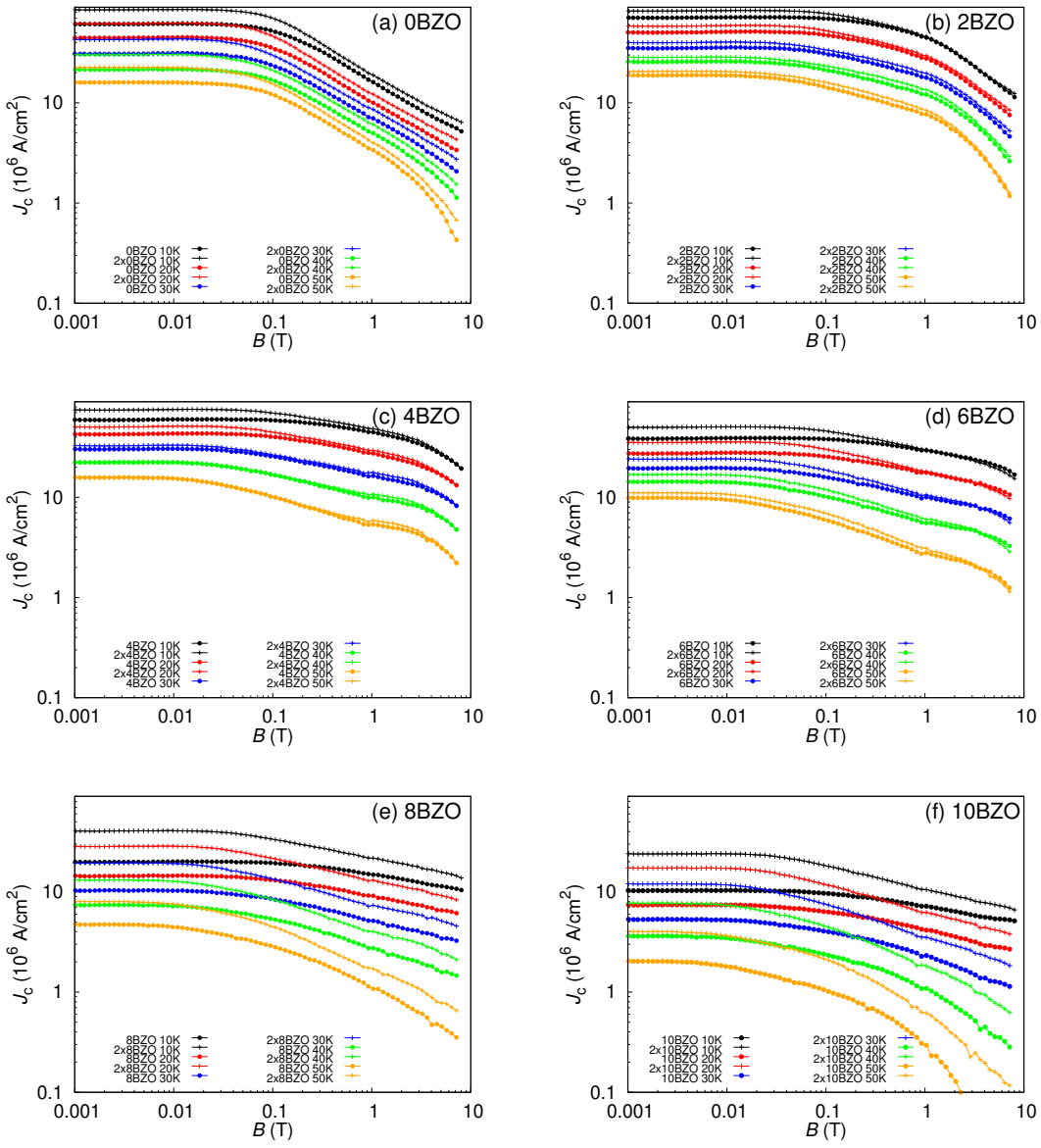

Figure 22. Critical current densities at varying magnetic fields and varying temperatures. The same color has been used to denote measurements done at the same temperature. Each graph shows the single and multilayered samples at a specific concentration of BZO at five different temperatures 10, 20, 30, 40 and 50 K.

When comparing the samples, we can see that 2x4BZO has the highest in-field J_c, but the improvement of J_c is not that great, when comparing 4BZO to 2x4BZO. However, when comparing samples with higher BZO concentration, we see a much larger improvement in the J_c values between single and multilayers. These improvements can be seen in figure 23. Here, it is more clearly shown that multilayering improves the J_c much more effectively at high concentrations of BZO. This is due to the fact that higher concentrations of BZO cause more structural issues and so the Ca-doping has more to fix than in lower concentrations of BZO.

As the film gets thicker, the strain in the crystal lattice causes an increasing number of defects, especially with the growth of the BZO nanorods as they may break or misalign as they get taller. The Ca-doped intermediary layer in a sense resets the building surface for the BZO nanorods and YBCO by relaxing the strain and promoting proper growth. Higher concentrations of BZO have a higher number of BZO nanorods and so when the Ca-doped layer improves the quality of each nanorod, the total amount of improvement is much larger. This is why the higher concentrations of BZO experience larger improvements in their J_c values than the lower concentrations. In the vicinity of the BZO nanorods, the YBCO quality suffers. The strain can induce oxygen vacancies in the interface between BZO and YBCO as well as degrading quality. This means that as we increase the number of BZO nanorods we also increase the amount of interface defects in the YBCO while decreasing the amount of properly grown YBCO. The Ca-doped intermediary layer has been shown to help with these by compensating for the oxygen deficiencies with mobile oxygen atoms, this can also be seen by the decrease in I_{ratio} seen in the XRD section. The Ca-doped layer also helps with the strain relaxation caused by the lattice parameter mismatch, this can be seen by the improvements in structural quality seen in the XRD section. The increase in J_c seen in the multilayer samples is due to the Ca-doped intermediary layer aiding in strain relaxation and compensating

for oxygen deficiencies in the YBCO-BZO interface.

3.3.4 Optimal multilayer structures in different magnetic fields and temperature ranges

The improvements shown in figure 23 may be slightly misleading. Although 8% and 10% BZO samples experienced the greatest improvements in J_c, the sample with the highest absolute J_c was 2x4BZO under most conditions. Figure 24 shows the sample with the highest J_c at different magnetic fields and temperatures. At zero and low-fields, the 2x0BZO sample has the highest J_c, this is due to the lack of BZO causing strain in the sample and the multilayer improving crystal quality and oxygen content. 2x2BZO was the best at magnetic fields around 1 T and 2 T at higher temperatures. This is due to the same reasons but with a capacity for vortex pinning allowing it to endure higher magnetic fields. For the rest of the measured ranges 2x4BZO proved to be the best sample. 2x4BZO is at a balance of having enough BZO nanorods for vortex pinning effectively, but not having so many that it negatively effects the crystal structure of the film. Values for J_c at 8 T were only obtained at a temperature of 10 K, and in at these conditions 4BZO had the highest J_c value.

3.3.5 Mechanisms behind increased critical current density

The dependence of J_c on the magnetic field at a set temperature can be described by equation (2) which was

$$J_c(B) \propto J_{c,0} \times B^{-\alpha},$$

where $J_{c,0}$ is the critical current density at zero-field and α is a unitless parameter which decreases as vortex pinning is increased. To obtain the best J_c values in in-field conditions these parameters must be balanced optimally, so that we have a high $J_{c,0}$ while still having effective pinning. The implementation of the BZO-doping

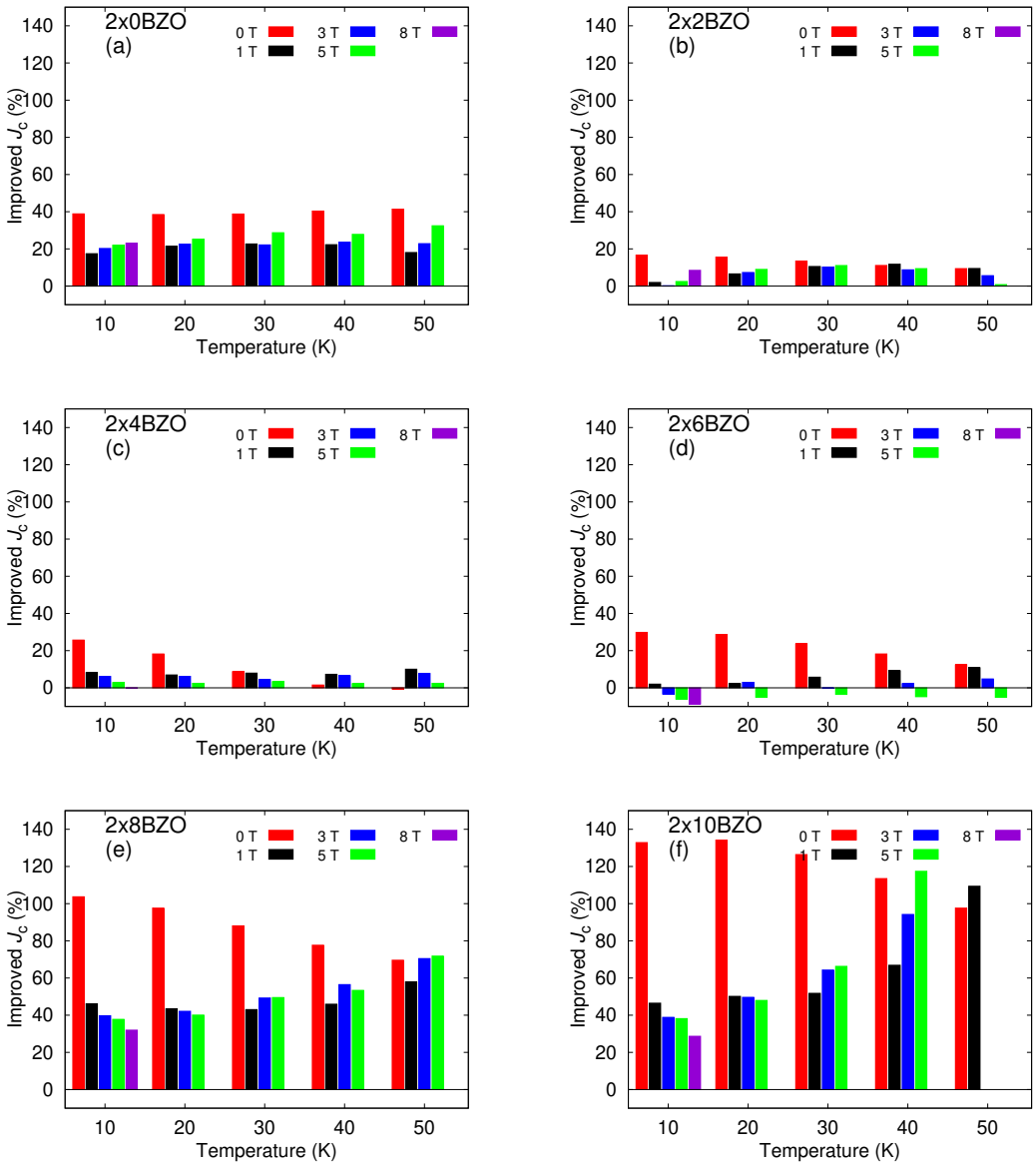

Figure 23. Improvement of J_c going from single layer to multilayer.

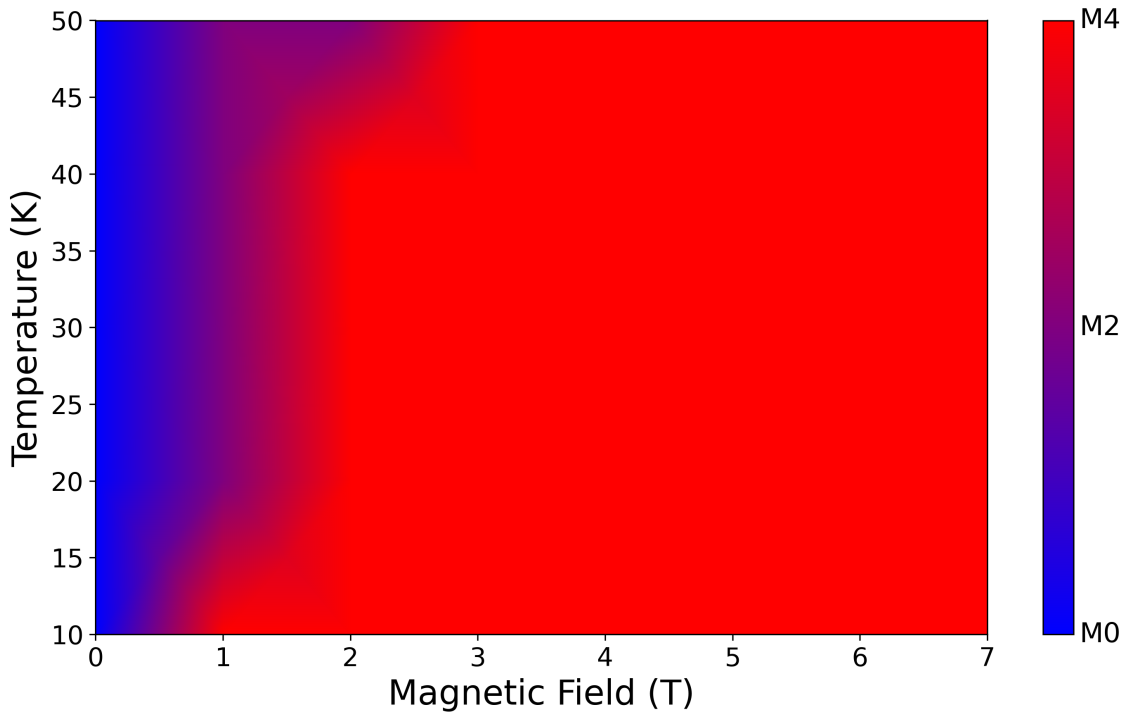

Figure 24. Sample with the highest absolute J_c at different temperatures and magnetic fields. M0 referes to 2x0BZO, M2 to 2x2BZO and M4 to 2x4BZO.

decreases the $J_{c,0}$ for two reasons, firstly the decrease of crystalline quality of the superconducting lattice, and secondly a decrease in superconducting cross sectional area.

Degradation of the crystalline quality decreases the J_c by reducing the mean free path of Cooper pairs (l) [26]. This is due to the increased number of lattice defects and abnormalities that will affect the electrons path, increasing electron scattering. This increase will affect the superconducting coherence length with the relation

$$\frac{1}{\xi} = \frac{1}{\xi_0} + \frac{1}{l}, \tag{5}$$

where ξ_0 is the clean limit superconducting coherence length [30]. The mean free path of Cooper pairs also influences the superconducting penetration depth

$$\lambda = \lambda_0 \sqrt{1 + \frac{\xi_0}{l}}, \tag{6}$$

where λ_0 represents the clean limit for superconducting penetration depth. With

this we can see that the characteristic lengths govern the J_c at zero-field as

$$J_{c,0} \propto \frac{1}{\lambda}[\frac{\Phi_0}{4\pi\mu_0\lambda^2}(\ln(\frac{\lambda}{\xi}) + \frac{1}{2}]. \tag{7}$$

This is the reason why crystalline quality affects the J_c at zero-field. The in-field J_c is governed by the effectiveness of the pinning centers, however, the $J_{c,0}$ still influences the in-field J_c by being the base from which it deviates. [5, 26]

The reduction in J_c as a result of reduced superconductive cross-sectional area caused by the inclusion of BZO is minimized by the use of the Ca-doped intermediary layer. The intermediary layer will reduce the pinning efficiency, as the BZO nanorods of different layers may not be perfectly aligned. However, the increase in crystalline quality and thus the increase in $J_{c,0}$ will make up for this trade-off. The seed-layer effect is being utilized in the first Ca-doped layer to absorb the stress caused by substrate induced strain. This gives the BZO-doped YBCO a smooth epitaxial interface to start its growth improving the crystalline quality [31]. The diffusion of mobile oxygen atoms into strain induced vacancies of the BZO-YBCO interface from the Ca-doped YBCO layer as seen in figure 18, also improve crystal quality and SC properties.

4 Summary and conclusion

The purpose of this thesis was to study the effects of incorporating Ca-doped YBCO spacer layers in BZO-doped YBCO multilayer coated conductor thin films. By finding ways to improve the J_c and H_c values of coated conductors, we can improve future designs of superconductors. The increase of J_c will allow more current to be transported in a smaller area and can be used to generate higher magnetic field in SC magnets. The increase of H_c allows for more varied applications of the SC in extreme conditions.

Previous research has shown that the incorporation of BZO in YBCO coated

conductors effectively pins magnetic flux lines that penetrate that material in the mixed state, increasing the H_c of the material. Ca-doped YBCO spacer layers have also been shown to improve the crystal quality in these CCs. In this thesis we are studying these improvements at varying concentrations of BZO.

Two sets of samples were fabricated using PLD to achieve epitaxial crystal growth. The first set of samples was the single layer samples of YBCO with BZO doping ranging from 0% to 10% in 2% increments. The second set was the multilayer set, which differs by having a Ca-doped layer in between the substrate and the first YBCO layer and between the first and second BZO-doped YBCO layer. Structural characteristics were measured and analyzed using XRD and AFM measurements. Magnetic and resistive measurements were performed using PPMS and aided by photolithography.

From the structural analysis we found that the addition of Ca-doped layers improves the crystal lattice quality and aids in oxygen saturation as seen by the decrease in I_{ratio} values. XRD results show decreases in microstrain and the FWHM for the (005) peaks of 2x2BZO and 2x4BZO samples in the 2θ-scan. Out-of-plane quality was assessed with rocking curve measurements and samples with Ca-doping had smaller $\Delta\omega_{005}$ values than those in their single layer counterparts. Improvements were also observed with the in-plane quality as assessed with a ϕ-scan. BZO growth quality was also assessed with measurements of $\Delta\omega_{002}$ and $\Delta\phi_{110}$, in which the multilayer samples were observed to have improved values. From the XRD measurements, we can conclude that the Ca-doping has aided in the formation of BZO nanorods, the crystal lattice structure, and in the oxygen saturation of the samples.

The first magnetic measurement performed was the magnetization as a function of temperature measurement. From this, we found that at low BZO concentrations the single layer samples had higher T_c, while at higher concentration of BZO the multilayer samples had higher T_c. Multilayered samples also had smaller ΔT_c values.

From the second magnetic measurement, we were able to calculate the J_c as a function of external magnetic field at different temperatures. From these results, we could clearly see that the J_c values are improved with the incorporation of Ca-doped intermediary layers. The multilayers had higher J_c values throughout the magnetic field and temperature ranges except for the 6BZO samples at high external fields. The greatest improvements in J_c were observed in the high concentrations of BZO. However, the highest absolute values for J_c were observed with the lower concentrations of BZO, with the 2x4BZO sample having the highest value in most conditions.

Photolithography was used to pattern the samples for resistivity measurements. A standard photolithography process was used to pattern the samples. After which a wire bonder was used to prepare them for resistivity measurements. Resistivity measurements were performed to determine more accurate T_c values for the samples. The results were similar to the magnetization measurements performed earlier.

Based on the measurements and analysis, the use of Ca-doped YBCO intermediary layers does improve the superconducting properties of BZO-doped YBCO thin films. These improvements will help with future designs of coated conductors in applications were high J_c, H_c and T_c are necessary. A possible application for these coated conductors, which can withstand high magnetic fields, is in fusion reactors, where there are multiple sets of SC magnets used to confine and control the plasma toroid, which is used to produce energy.

Future research should be done into how the number of layers and layer thickness affect the superconducting properties of YBCO. This will help in designing coated conductors with the absolute highest J_c values. Another challenge that needs to be faced is the production of high-quality coated conductors that are of appropriate size for applications, in an economical fashion.

References

[1] H. Onnes, Leiden Comm. **120b, 122b, 124c**, (1911).

[2] J. G. Bednorz and K. A. Müller, Z. Phys. B **64**, 189 (1986).

[3] S. Tanaka, The Japan Society of Applied Physics **1**, 4 (2001).

[4] M. K. Wu *et al.*, Phys. Rev. Lett. **58**, 908 (1987).

[5] M. M. Aye *et al.*, Supercond. Sci. Technol. **35**, 075006:1 (2022).

[6] M. M. Aye *et al.*, IEEE Transactions on Applied Superconductivity **35**, (2024).

[7] D. van Delft, Physica C: Superconductivity **479**, 30 (2012).

[8] J. E. Hirsch, Physica Scripta **85**, 035704 (2012).

[9] E. H. Brandt, Rep. Prog. Phys. **58**, 1465 (1995).

[10] J. Bardeen, L. N. Cooper, and J. R. Schrieffer, Physical Review **108**, 1175 (1957).

[11] R. Wesche, *Springer Handbook of Electronic and Photonic Materials* (Springer , 2006).

[12] C. P. Poole Jr., H. A. Farach, R. J. Creswick, and R. Prozorov, *Superconductivity, Second Edition* (Academic Press , 2007).

[13] E. Rivasto, *Vortices and artificial defects in superconducting thin films: Increasing the critical current densities via optimization of multilayer structures* (Turun yliopisto, University of Turku , 2023), p. 190.

[14] M. M. Aye, *Optimized pinning in high-temperature superconductor thin films* (Turun yliopisto, University of Turku , 2024), p. 118.

[15] P. Zhang *et al.*, in *Titanium for Consumer Applications*, edited by F. Froes, M. Qian, and M. Niinomi (Elsevier , 2019), pp. 279–296.

[16] J. D. Jorgensen *et al.*, Phys. Rev. B **41**, 1863 (1990).

[17] J. D. Jorgensen *et al.*, Phys. Rev. B **36**, 3608 (1987).

[18] J. L. MacManus-Driscoll *et al.*, Nat. Mater. **3**, 439 (2004).

[19] G. Iannone *et al.*, Cryogenics **109**, 103116 (2020).

[20] D. B. Chrisey and G. K. Hubler, *Pulsed Laser Deposition of Thin Films* (John Wiley Sons Inc. , 1994).

[21] M. M. Aye *et al.*, ACS Applied Nano Materials **5**, 18159 (2022).

[22] G. F. Harrington and J. Santiso, Journal of Electroceramics **47**, 141 (2021).

[23] H. P. Wiesinger, F. M. Sauerzopf, and H. W. Weber, Physica C **203**, 121 (1992).

[24] M. M. Aye, E. Rivasto, H. Huhtinen, and P. Paturi, Cryst. Growth Des. **24**, 4545 (2024).

[25] J. D. Jorgensen, P. Lightwood, and S. Pei, Supercond. Sci. Technol. **4**, S11 (1991).

[26] P. Paturi and H. Huhtinen, Supercond. Sci. Technol. **35**, 065007:1 (2022).

[27] M. M. Aye *et al.*, IEEE T. Appl. Supercond. **33**, 6601806:1 (2023).

[28] A. Tuomola *et al.*, J. Phys. Cond. Mat. **35**, 475001:1 (2023).

[29] R. Wiesendanger and H.-J. Guntherodt, Phys. Rev. Lett. **65**, 247 (1990).

[30] A. Pippard, Physica **19**, 765 (1953).

[31] Y. Yao *et al.*, Appl. Surf. Sci. **442**, 658 (2018).